UNIVERSITY OF CALIFORNIA

Santa Barbara

Temperature-Dependent Behavior of Organic Semiconductors

A dissertation submitted in partial satisfaction of the

requirements for the degree Doctor of Philosophy

in Chemistry

by

Martin Thomas Seifrid

Committee in charge:

Professor Guillermo Bazan, Chair

Professor Thuc-Quyen Nguyen

Professor Javier Read de Alaniz

Professor Rachel Segalman

September 2019

The dissertation of Martin Thomas Seifrid is approved.

_____

Rachel Segalman

_____

Javier Read de Alaniz

_____

Thuc-Quyen Nguyen

_____

Guillermo Bazan, Committee Chair

July 2019

Temperature-Dependent Behavior of Organic Semiconductors

ACKNOWLEDGEMENTS

The work described herein would not have been possible without the help and support of many people over the course of the last five years. Although I have done my best to include everyone who has played a role in supporting, encouraging and pushing me, I may have missed some of them.

While the journey to a PhD is by no means an easy one, with challenges of many different types along the way, I don't think there is a better place to be a graduate student than at UCSB. The faculty, staff and students together create an atmosphere that fosters collaboration and excellent research, along with world-class facilities and arguably the best campus location in the world.

First of all, I want to thank my advisor, Gui Bazan, who has taught me a lot in the course of my time in his group. Gui has an exceptional knack for identifying important challenges and coming up with creative solutions to problems; both skills that I have done my best to learn and incorporate into my own research. He has also been a great mentor in terms of sharing his experience in academia, encouraging my growth as a scientist and helping me navigate my career at UCSB and afterward. Quyen Nguyen, with whose group I have had the fortune to work very closely, has also been a tremendous source of guidance and support throughout my time at UCSB. Even though I was not in her group, Quyen always found time to help me by providing feedback on the directions of my projects, as well as helping me prepare for interviews. I would also like to thank my other committee members, Javier Read de Alaniz and Rachel Segalman, who have always offered valuable guidance when I met with them.

I would also like to thank the many grad students and post-docs who have mentored or worked with me because without them, I could not have gotten to this point. When I first joined the Bazan group, Jessi Coughlin and Xiaofeng Liu took me under their wing and taught me how to be a successful grad student and a good labmate. Michael Ford, Jaewon Lee, Caitlin McDowell, Hung Phan, Zach Rengert and Cheng Zhou have also all played an important role– as collaborators, colleagues, mentors and friends– in my development as a grad student and scientist. Alex Moreland, Brett Yurash and Alex Lill played an important part as great sources of feedback or ideas, as well as being great friends. More recently, I had the chance to work with Brad Chmelka and Manju Reddy. Both Manju and Brad are excellent scientists, collaborators, mentors, from whom I have tried to learn as much as possible in the time that we've known each other. I have also tremendously benefitted from their enthusiastic support and encouragement. There are many other people from whom I have learned a lot and who have made CPOS and UCSB a great place to be over the past five years: Bing Wang, Cheng-Kang Mai, Chenyao Nie, Dirk Leifert, Hengjin Yan, Jakkarin Limwongyut, Jinayu Yuan, John Markiewicz, Lingyun Zhou, Luana Llanes, Mark Burgers, Ming Wang, Samantha McCuskey, Stephanie Fronk, Xi Liu, Yasu Hasegawa, Ziyue Zhu, Akcheta Karki, Ben Luginbuhl, Chris Proctor, Jianfei Huang, Joachim Vollbrecht, Katie Rosenthal, Michael Hughes, Niva Ran, Seo-Jin Ko and Viktor Brus.

I am grateful to my parents for instilling in me the work ethic, drive, curiosity and passion that have aided me in the journey to obtaining my PhD, as well as for their support and love throughout life. Finally, I couldn't have made it through grad school without Crystal's endless support, encouragement and love.

VITA OF MARTIN THOMAS SEIFRID
June 2019

EDUCATION

Doctor of Philosophy in Chemistry, University of California, Santa Barbara, June 2019 (expected)

Bachelor of Sciences in Chemistry, University of Southern California, May 2014 (cum laude)

PROFESSIONAL EMPLOYMENT

2015-Present: Graduate Student Researcher, Department of Chemistry, University of California, Santa Barbara

2014-2015: Teaching Assistant, Department of Chemistry, University of California, Santa Barbara

2013-2014: Research Assistant, Department of Chemistry, University of Southern California

PUBLICATIONS

M. T. Seifrid, G. N. M. Reddy, C. Zhou, B. F. Chmelka, and G. C. Bazan, Direct Observation of the Relationship Between Molecular Topology and Bulk Morphology for a Pi-Conjugated Material. *J. Am. Chem. Soc.* **2019**, *141* (13), 5078-5082.

Y. Xu, J. Yuan, S. Zhou, M. Seifrid, L. Ying, B. Li, F. Huang, G. C. Bazan, and W. Ma, Ambient Processable and Stable All-Polymer Organic Solar Cells. *Adv. Funct. Mater.* **2019**, 1806747.

A. Karki, G.-J. A. H. Wetzelaer, G. N. M. Reddy, V. Nádazdy, M. Seifrid, F. Schauer, G. C. Bazan, B. F. Chmelka, P. W. M. Blom, and T.-Q. Nguyen, Unifying Energetic Disorder from Charge Transport and Band Bending in Organic Semiconductors. *Adv. Funct. Mater.* **2019** *0* (0), 1901109.

A. T. Lill, A. F. Eftaiha, J. Huang, H. Yang, M. Seifrid, M. Wang, G. C. Bazan, and T.-Q. Nguyen, High-k Fluoropolymer Gate Dielectric in Electrically Stable Organic Field-Effect Transistors. *ACS Appl. Mater. Interfaces* **2019** *11* (17), *15821-15828.*

J. Lee, S.-J. Ko, H. Lee, J. Huang, Z. Zhu, M. Seifrid, J. Vollbrecht, V. Brus, H. Wang, K. Cho, T.-Q. Nguyen, and G. C. Bazan, Side Chain Engineering of Non-Fullerene Acceptors for Near-Infrared Organic Photodetectors and Photovoltaics. *ACS Energy Lett.* **2019**, *4* (6), 1401-1409.

B. Yurash, D. Leifert, G. N. M. Reddy, D. X. Cao, S. Biberger, V. V. Brus, M. Seifrid, P. J. Santiago, A. Köhler, B. F. Chmelka, G. C. Bazan, and T.-Q. Nugyen, Atomic-Level Insight into the Post Synthesis Bandgap Engineering of a Lewis Basic Polymer Using the Lewis Acid Tris(pentafluorophenyl)borane. *Chem. Mater.* **2019** *in press*.

M. T. Seifrid, S. D. Oosterhout, M. F. Toney, and G. C. Bazan, Kinetic Versus Thermodynamic Orientational Preferences for a Series of Isomorphic Molecular Semiconductors. *ACS Omega* **2018**, *3* (8), 10198–10204.

J. Lee, S.-J. Ko, M. Seifrid, H. Lee, C. McDowell, B. R. Luginbuhl, A. Karki, K. Cho, T.-Q. Nguyen, and G. C. Bazan, Design of Nonfullerene Acceptors with Near-Infrared Light Absorption Capabilities. *Adv. Energy Mater.* **2018**, 1801209.

J. Lee, S.-J. Ko, M. Seifrid, H. Lee, B. R. Luginbuhl, A. Karki, M. Ford, K. Rosenthal, K. Cho, T.-Q. Nguyen, and G. C. Bazan, Bandgap Narrowing in Non-Fullerene Acceptors: Single Atom Substitution Leads to High Optoelectronic Response Beyond 1000 nm. *Adv. Energy Mater.* **2018**, *8* (24), 1801212.

M. P. Hughes, K. D. Rosenthal, N. A. Ran, M. Seifrid, G. C. Bazan, and T.-Q. Nguyen, Determining the Dielectric Constants of Organic Photovoltaic Materials Using Impedance Spectroscopy. *Adv. Funct. Mater.* **2018**, *28* (32), 1801542.

C. McDowell, K. Narayanaswamy, B. Yadagiri, T. Gayathri, M. Seifrid, R. Datt, S. M. Ryno, M. C. Heifner,V. Gupta, C. Risko, S. P. Singh, and G. C. Bazan, Impact of Rotamer Diversity on the Self-Assembly of Nearly Isostructural Molecular Semiconductors. *J. Mater. Chem. A* **2018**, *6* (2), 383–394.

M. Seifrid, M. J. Ford, M. Li, K. M. Koh, P. Trefonas, and G. C. Bazan, Electrical Performance of a Molecular Organic Semiconductor Under Thermal Stress. *Adv. Mater.* **2017**, *29* (12), 1605511.

B. Wang, G. Feng, M. Seifrid, M. Wang, B. Liu, and G. C. Bazan, Antibacterial Narrow-Band-Gap Conjugated Oligoelectrolytes with High Photothermal Conversion Efficiency. *Angew. Chem. Int. Ed.* **2017**, *56* (50), 16063–16066.

C. Zhou, Q. Cui, C. McDowell, M. Seifrid, X. Chen, J.-L. Brédas, M. Wang, F. Huang, and G. C. Bazan, Topological Transformation of π-Conjugated Molecules Reduces Resistance to Crystallization. *Angew. Chem. Int. Ed.* **2017**, *56* (32), 9318–9321.

M. Wang, M. J. Ford, C. Zhou, M. Seifrid, T.-Q. Nguyen, and G. C. Bazan, Linear Conjugated Polymer Backbones Improve Alignment in Nanogroove-Assisted Organic Field-Effect Transistors. *J. Am. Chem. Soc.* **2017**, *139* (48), 17624–17631.

S. L. Fronk, Y. Shi, M. Seifrid, C.-K. Mai, C. McDowell, and G. C. Bazan, Chiroptical Properties of a Benzotriazole–Thiophene Copolymer Bearing Chiral Ethylhexyl Side Chains. *Macromol.* **2016**, *49* (24), 9301-9308.

J. Facendola, M. Seifrid, J. S. Siegel, P. I. Djurovich, and M. E. Thompson, Synthesis and Characterization of Phosphorescent Platinum and Iridium Complexes with Cyclometalated Corannulene. *Dalton Trans.* **2015**.

L. F. Gomez, K. R. Ferguson, J. P. Cryan, C. Bacellar, R. M. P. Tanyag, C. Jones, S. Schorb, D. Anielski, A. Belkacem, C. Bernando, *et al.*, Shapes and Vorticities of Superfluid Helium Nanodroplets. *Science* **2014**, *345* (6199), 906–909.

PATENTS

U.S. Patent US 2019 / 0157581 A1 "Narrow bandgap non-fullerene acceptors and devices including narrow bandgap non-fullerene acceptors"

CONFERENCES AND PRESENTATIONS

M. Seifrid, G. N. M. Reddy, C. Zhou, B. F. Chmelka, and G. C. Bazan, "Direct Observation of the Relationship Between Molecular Topology and Bulk Morphology for a π-Conjugated Material" *14th International Symposium on Functional π-Electron Systems*. Berlin, Germany. June 2-8, 2019. Poster. (expected)

M. Seifrid, G. N. M. Reddy, B. F. Chmelka, and G. C. Bazan, "Atomic-Level Resolution of the Solid-State Organization of Organic Semiconductors" *Emerging Material Technologies Summit 2018*. Hanoi, Vietnam. November 4-8, 2018. Talk.

M. Seifrid, J. Lee, S.-J. Ko, T.-Q. Nguyen, and G. C. Bazan, "Materials Design & Energetic Considerations for Narrow Bandgap Non-Fullerene Organic Solar Cells" *9th International Conference on Excited State Processes in Electronic and Bio Nanomaterials 2018*. Santa Fe, NM, USA. June 4-7, 2018. Talk.

M. Seifrid, J. Lee, S.-J. Ko, T.-Q. Nguyen, and G. C. Bazan, "New Opportunities in Organic Solar Cells" *Institute for Energy Efficiency Emerging Technologies Review*. Santa Barbara, CA, USA. May 10, 2018. Talk.

M. Seifrid, M. J. Ford, M. Li, K. M. Koh, P. Trefonas, and G. C. Bazan, "Characterization of Electrical Performance in a Molecular Organic Semiconductor Under Thermal Stress" *Zing Organic Semiconductors Conference 2016*. Dubrovnik, Croatia. September 23-25, 2016. Talk.

AWARDS

Graduate Student Assembly Conference Travel Grant, UCSB, 2019

Academic Senate Doctoral Student Travel Grant, UCSB, 2018

IUPAC Bursary recipient, Emerging Material Technologies Summit, 2018

Outstanding Service to the Department Award, UCSB, 2017 & 2018

Chemistry Department Honors, USC, 2014

Dornsife College of Letters, Arts & Sciences Dean's List, Fall 2012 – Spring 2014

Student Opportunities for Academic Research, Fall 2012

Summer Undergraduate Research Fund, Summer 2011 & 2012

ACTIVITIES AND INVOLVEMENT

Graduate Students for Diversity in Science (GSDS)	2014 – Present
Ventura High School visits to UCSB	Spring 2015 & 2017
SciTrek volunteer	Fall 2014 & 2015

ABSTRACT

Understanding Temperature-Dependent Behavior of Organic Semiconductors

by

Martin Thomas Seifrid

Many properties of organic semiconductors, such as charge transport or optical absorbance, are governed by the solid-state organization of the material, which is in turn determined by its chemical structure. Developing a fundamental understanding of molecular features that can be used to control the solid-state properties of organic semiconductors is key to designing materials with improved performance or unique new properties. In my research, I have employed a diverse set of techniques, such as theory, experiment and device characterization, to better understand the relationship between molecular structure and solid-state properties of molecular organic semiconductors. Herein, the relationship between the chemical structure of molecular and oligomeric organic semiconductors and their response to thermal stresses and changes in temperature are described. First, I will describe the tolerance of an organic field-effect transistor to operation at temperatures up to 200 ºC and over multiple high-temperature cycles, with only slight changes in charge carrier mobility and properties. The active layer of this device is composed of an oligomeric organic semiconductor whose structure is very similar to that of two well-known ambipolar conjugated polymers. Heating to 200 ºC or above results in appearance ambipolar charge

transport in the oligomeric active layer as well. Then, the solid-state organization of a nearly isostructural series of oligomeric organic semiconductors–including the material discussed above–is characterized. As-cast, the first half of the series orients edge-on relative to the substrate while the second half is oriented face-on. This difference is likely due to kinetic trapping during the spin-coating process because melt-annealing of thin films of the four different materials results in edge-on orientation of crystallites for all four molecules. Finally, I describe a combined theoretical and experimental approach to probing aspects of molecular organization and topology based on solid-state NMR. Using this approach, a previously hypothesized change in molecular shape upon crystallization of a molecular organic semiconductor is confirmed. The novel molecular design element of a tail-to-tail couple hexyl-bithiophene core removes the trade-off between solubility and solid-state order in molecular semiconductors.

TABLE OF CONTENTS

LIST OF FIGURES

I. Testing the Limits of Device Operation at Elevated Temperature

A. Thermal stability in organic semiconductor devices

Organic semiconductors (OSCs) are held together by weaker forces relative to their inorganic counterparts.[1] While typical inorganic semiconductors are bound by covalent bonds that provide rigid lattices, the stability of organic semiconducting materials is determined by intermolecular interactions, such as van der Waals forces, electrostatic forces and hydrogen bonding. OSCs therefore tend to have lower melting points and less stable thin films.[2] Furthermore, typical morphological characteristics of the two main types of OSCs – polymers and small molecules – may exhibit different relative advantages and drawbacks when considering function under thermal stress. Whereas molecular systems can be highly crystalline,[3–6] conjugated polymer solid contain a significant portion of amorphous domains,[7,8] which may be locations where heat-induced structural instability begins.[9] However, due to their comparatively smaller size, molecular systems with similar units often have lower melting points.[10,11] These differences in melting temperatures, purity, and the content of ordered and disordered domains impact electrical performance at high temperatures.

How temperature impacts OSC devices is of growing interest as the importance of a compact form factor becomes more significant in technological applications and as heat dissipation becomes increasingly relevant.[12–15] The integration of organic electronics into more diverse applications, such as in automotive technology and biomedical devices, creates a demand for materials that exhibit functional stability across a broad temperature range.

However, only a limited number of studies have been carried out on the influence of temperature on the stability of organic field-effect transistors (OFETs). Early efforts focused on polythiophene-[16] and pentacene-based[17] devices and showed that these systems experienced a decrease in hole mobilities of up to multiple orders of magnitude when operating the OFETs at elevated temperatures. More recent investigations with pentacene-[18] and perylenediimide-based[19] devices have focused more on device stability. To what extent thermal stress cycles, such as those encountered in commercial device applications, impact OFET stability remains under-explored. These studies are also fundamentally different from previous reports on temperature-dependent mobilities that have been predominantly carried out to extrapolate the activation energy of hopping transport in organic semiconductors.[20–26]

The compound X2 (Figure 1-1) was selected for study due to its molecular structure and desirable thermal properties. Its conjugated backbone, composed of alternating electron-rich and electron-deficient fused heterocycles is consistent with the traditional model of molecular design for organic semiconductors, where the backbone is designed to be as planar and rigid as possible, with alkyl sidechains to make it solution-processable. The melting temperature of X2 is comparatively high (269 ºC),[35,36] which makes it possible to study charge carrier transport under conditions of thermal and electrical stress, and its organizational preferences lead to a predominantly edge-on orientation,[37] which is well-suited to OFET applications. It is worth noting, however, despite extensive morphological studies there is no complete understanding of how bulk thermal stability, obtained from differential scanning calorimetry, correlates to the stability of OFETs. Therefore, in this chapter, I will examine the charge transport of X2 at high temperature.

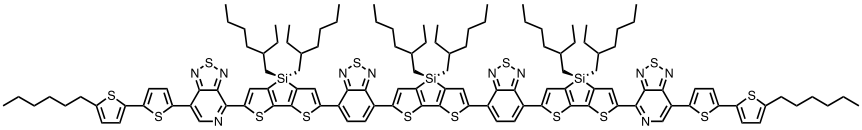

Figure 1-1. Molecular structure of X2.

B. Results and discussion

Bottom gate, bottom contact OFETs were fabricated with a simple general structure of Si/SiO_2/Au contacts/X2. Prior to deposition of X2, the substrates were treated with a decyltrichlorosilane monolayer to passivate the semiconductor-dielectric interface. Following monolayer treatment, the semiconductor was deposited from a chloroform solution by spin-coating onto the substrate.

As described in more detail below, thermal stress (i.e. subjecting the OFET device to elevated temperatures) can lead to changes in the current/voltage characteristics. One manifestation of thermal stressing effects is hysteresis in the forward and backward sweep of the transfer measurements, where the gate voltage is swept from positive to negative for the forward scan and subsequently swept negative to positive for the backward scan. This hysteresis was quantified by the difference in the calculated threshold voltage for the forward and back scans, namely ΔV_T^{fb}. Values for the threshold voltage for the forward and back scans were obtained by fitting to the square root of the absolute value of the source-drain current (I_{SD}) in each direction. I applied the fit to the broadest I_{SD}/V_G range while avoiding device artifacts, such as contact resistance or a double slope, that do not necessarily reflect carrier mobility (see Figure 1-S1).[38–40]

I will first discuss the impact of thermal annealing on the electrical properties measured at room temperature (RT). These studies involved annealing the devices for 10 minutes at temperatures ranging from 50 ºC to 250 ºC. Devices that were measured as-cast (Figure 1-2a), as well as those annealed at 50 ºC (Figure 1-S2), show negligible hysteretic behavior: ΔV_T^{fb} = -1 ± 0.3 V for the as-cast film. Thermal annealing above 100 ˚C leads to more pronounced differences in the forward and back scans; the device annealed at 200 ˚C exhibits ΔV_T^{fb} = -6 ± 0.2 V (Figure 1-2a). Hole mobilities (μ_h) were calculated from plots of the square root of the absolute value of I_{SD} ($|I_{SD}|^{1/2}$) vs. gate voltage (V_G) (Figure 1-S1), and the results are incorporated in Figure 1-2c. Regardless of the thin film annealing temperature, even up to 250 ˚C, all OFET mobilities are in the range between 0.009 ± 0.0002 cm^2/Vs to 0.02 ± 0.001 cm^2/Vs, thereby demonstrating a remarkable resilience toward heat treatments.

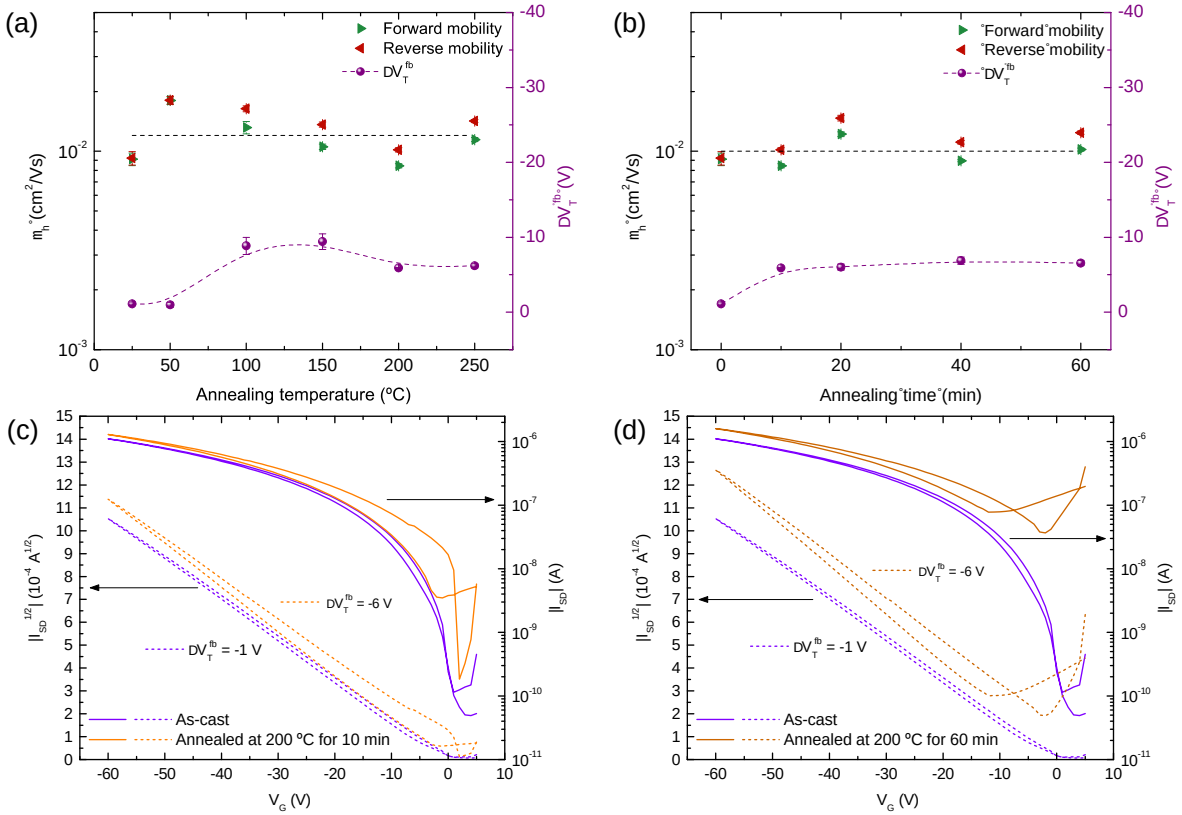

Figure 1-2. Effects of annealing on the properties of X2 OFETs. a) Transfer characteristics of typical as-cast devices and devices annealed at 200 ˚C for 10 minutes. b) Comparison of transfer characteristics of as-cast devices and those annealed for 60 minutes at 200 ºC. c) Devices annealed for 10 min at up to 250 ºC show negligible changes in mobility and ΔV_T^{fb} variations of -6 V to -9 V. d) Annealing at 200 ºC for up to 1 hour does not significantly affect hole mobility or hysteretic behavior in X2 OFETs.

OFETs were heated at 200 ºC for different time intervals (Figure 1-S3) up to one hour in order to investigate how the duration of heating impacts performance. As shown in Figure 1-2d, μ_h does not vary significantly with annealing time. Mobilities for both forward and back scans remained relatively unchanged (between 0.008 ± 0.0001 cm^2/Vs and 0.015 ± 0.0005 cm^2/Vs). There is also essentially no change in hysteresis between devices that were annealed for only 10 minutes (ΔV_T^{fb} = -6 ± 0.1 V) and those annealed for an hour (ΔV_T^{fb} = -6 ± 0.4 V). Examination of the transfer curves of representative devices in Figures 1-2a and 1-2b reveals that while the as-cast devices behave as a unipolar p-type semiconductor,

annealing creates emergent ambipolar behavior (Figure 1-S4). In Figure 1-2b, unipolar characteristics are assigned based on the low current ($|I_{SD}| < 10^{-9}$ A) measured in the voltage range for electron doping, $V_G > 0$. Ambipolar characteristics are revealed by the higher current ($|I_{SD}| \sim 10^{-7} - 10^{-6}$ A) in the same voltage range. This increase in current leads to changes in the on-off ratios of the forward and backward scans ($On/Off_{F/B}$). For as-cast devices, these ratios are On/Off_F and $On/Off_B \sim 10^4$, while the on-off ratios of the devices heated to 200 ºC for 60 min are $On/Off_F \sim 10^2$ - 10^3 and $On/Off_B \sim 30$. The similarity in molecular structure between X2 and ambipolar polymers such as PCPDTBT and PCDTPT suggests electron transport in X2 should be accessible.[27,29,31,32] Given that the hole mobility changes are not significant and show little variation, it seems reasonable that annealing at 200 ºC modifies interfacial properties at the source and drain contacts in such a way that they reduce barriers to electron injection.[41] This hypothesis is supported by variable temperature grazing incidence wide-angle X-ray spectroscopy (GIWAXS), as discussed below.

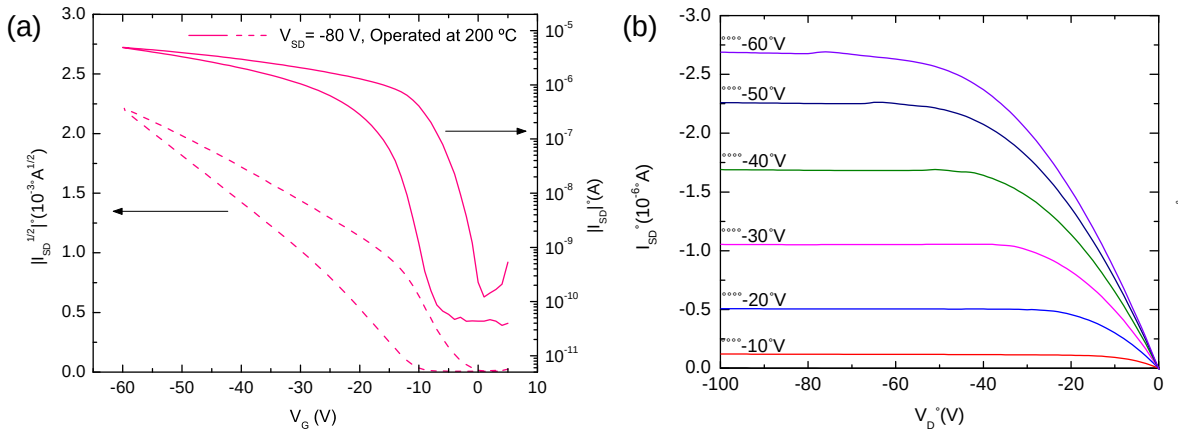

Figure 1-3. Representative transfer (a) and output (b) curves of annealed devices operated at 200 ºC following a 10 minute pre-annealing step.

Next, I studied the charge transport characteristics of X2 OFETs during operation at high temperature. Devices remained functional when operated at 200 ºC, albeit with more noticeable hysteretic behavior (ΔV_T^{fb} = -20 ± 4 V), as shown by the transfer and output curves in Figure 1-3. It is noteworthy that even at 200 ºC the output curves still reflect excellent device characteristics, including good saturation behavior (Figure 1-S5). Like the annealed devices, those operated at high temperature show lower currents on the back scans. However, the maximum current is larger, which may be reasonably explained by the thermally-activated hopping nature of charge transport through OSCs.[42–45] To examine if hysteretic behavior is irreversible, X2 OFETs were subjected to three cycles, during which the devices were measured at 200 ºC and subsequently at RT after being allowed to cool down (Figure 1-4). The ΔV_T^{fb} value of ~ -1 V for as-cast devices was used to provide a baseline measure for the change in hysteresis due to high temperature operation. Upon initial device measurement at 200 ºC, devices displayed hysteretic behavior, with ΔV_T^{fb} = -30 ± 7 V. Pre-annealed devices, on the other hand, were significantly less hysteretic (ΔV_T^{fb} = -20 ± 4 V). Retesting the devices at RT showed a change in behavior from the initial conditions of the devices (ΔV_T^{fb} = -5 ± 0.2 V). During the second cycle of high temperature operation, there is significantly less hysteresis, which does not change with the third cycle. Similar behavior was observed upon retesting of the OFETs after the second and third cycles (ΔV_T^{fb} = -4 ± 0.2 V). The effect of voltage scan rate on current-voltage hysteresis in devices subjected to the cycle described above was also explored (Figure 1-S6). It was found that scan rate does not significantly affect hysteresis or charge carrier mobility measured at room temperature. However, measurements during operation at high temperature show that

hysteresis decreases with increasing scan speed. The similarity in ΔV_T^{fb} between OFETs measured in cycles 2 and 3 and the annealed devices operated at 200 ºC indicates that the larger hysteresis of devices measured in the first heating cycle is likely due to the additive effects of high temperature operation and annealing. A thermal pre-annealing step therefore can be used to provide devices with predictable properties. Semiconducting thin films of X2 are therefore stable to the application of a large electric field while under significant thermal stress.

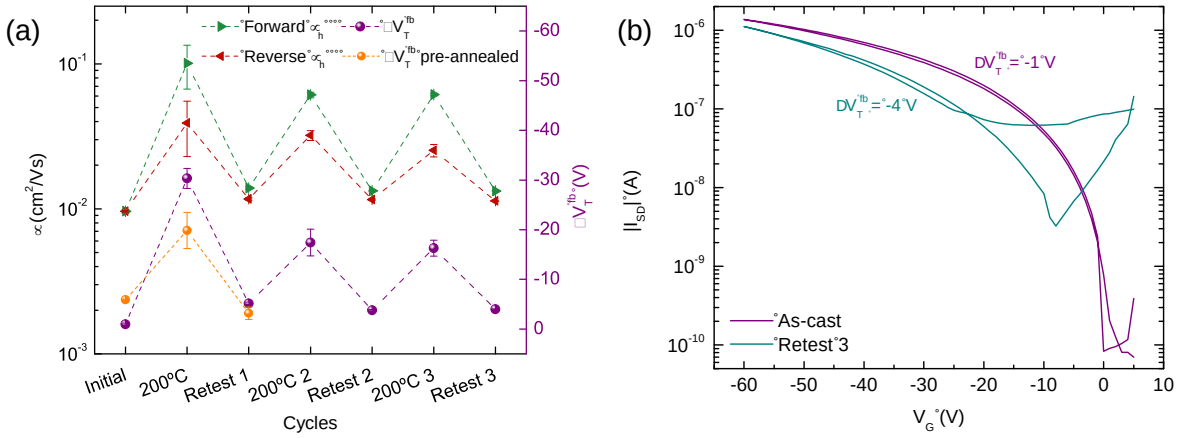

Figure 1-4. X2 OFETs are stable to multiple cycles of high temperature operation. a) Hole mobility and ΔV_T^{fb} characteristics of OFETs through the course of three cycles of operation at 200 ºC and after return to room temperature. b) Representative transfer curves of OFETs before application of any thermal stress and after the third high temperature (200 ˚C) operation cycle.

In-situ GIWAXS measurements were performed on the X2 films with the intent to probe morphological rearrangements that may occur within crystallites through heating.[46] Measurements at RT and 200 ºC (Figures 1-S8 – 1-S10) show little change in the position of the in-plane π-π stacking peak. At RT and 50 ºC, the peak maximum is 1.76 Å^{-1}, while at 200 ºC, the peak maximum is 1.72 Å^{-1}. This corresponds to an increase in π-π stacking distance of only 0.1 Å, attributable to thermal expansion of the lattice. At RT, the out-of-

plane lamellar stacking peak maximum is 0.4 $Å^{-1}$. Upon heating to 50 ºC and 200 ºC it decreases to 0.38 $Å^{-1}$, and 0.34 $Å^{-1}$, respectively. Cooling back to 50 ºC results in the peak shifting to 0.36 $Å^{-1}$. These changes, which represent a real-space range of ~2.8 Å, are consistent with an expanded lattice, which is unlikely to yield higher mobilities on the basis of weaker intermolecular electronic coupling. The larger mobilities at elevated temperatures can therefore be attributed to the conventional picture of hopping transport. The GIWAXS characterization examines only the fraction of the film that is crystalline; as such, it is possible that changes within the disordered domains or grain boundaries are responsible for the observed changes in charge transport behavior.

C. Conclusion

The molecular organic semiconductor X2 was chosen on the basis of its high melting point and tendency to form ordered thin films. Hole mobility is relatively constant throughout all the conditions that were examined. This stability is especially important, as significant changes due to variations in temperature under real-world conditions would result in difficult to manage device characteristics. The greater stability of charge transport in X2 compared to those of polythiophene- and pentacene-based OFETs may be attributed to its intermediate dimensions. Specifically, the decrease in performance of polythiophene OFETs at high temperature has been attributed to backbone distortions that limit the conjugation length in amorphous regions between crystallites,[16] while the decrease in performance of the pentacene has been explained in terms of partial sublimation, resulting in coarsening of the crystal grains.[17] A relatively high degree of order in the solid state may prevent such conformational and morphological changes in X2 thin films. The larger

molecular weight, in comparison to pentacene, prevents sublimation from causing thin film degradation. Device operation at elevated temperature leads to increased hysteretic behavior between the forward and back scans, although the values measured at 200 ºC are not unlike those of other OFETs reported at room temperature.[40,47–52] These studies have also revealed unexpected features, for example exposure to high temperature, followed by measurement at ambient temperature, turns on electron current in the device. The device characteristics at RT measured after operation at 200 ºC are similar to those of devices annealed at 200 ºC. Furthermore, their transfer curves display similar characteristics. These observations suggest that the appearance of ambipolar charge transport, characterized by increased off current and decreased on/off ratios, is due to the effects of thermal annealing alone. The similarity between X2 OFETs submitted to these two different conditions also suggests that there is little, if any, effect of the application of an electric field or current at high temperature. It is also important to note that no such ambipolar behavior is seen during operation of the OFETs at high temperature. The current thinking is that electron injection is most reasonably related to structural or chemical changes at the semiconductor/contact interface. Why this electron injection is temperature-dependent and depends in a counterintuitive way relative to temperature is not yet understood. Despite these uncertainties, the accumulated set of observations provides an encouraging perspective for the use of OSCs in applications that experience a wide temperature range. They also point to the need to further understand how molecular structure is related to specific bulk or thin-film properties upon changes in temperature in organic semiconducting materials.

D. Experimental and Supplementary Information

Device fabrication: Source and drain contacts (5 nm Ni/50 nm Au) were deposited using a standard two-step photolithography process onto Si/SiO_2 (300 nm) substrates. Before deposition, the pre-patterned substrates were cleaned by sonication in acetone and isopropanol for 3 minutes each, and were then dried in an oven under ambient atmosphere at 120 ºC for 30 minutes. The substrates were treated with UV-O_3 for 30 minutes. Subsequently, the substrates were passivated by refluxing in a 1 vol% solution of decyltrichlorosilane (Gelest Chemicals) in toluene at 80 ºC for 30 minutes. Afterward, the substrates were rinsed and sonicated in fresh toluene.[54] Films were deposited immediately after by spin-coating chloroform solutions of X2 (5 mg/mL) at 2500 rpm for 60 s.

Device characterization: The mobility of blend devices was obtained by fitting the following equation to the saturation regime transfer characteristics: $I_{SD} = (W/2L)C_i\mu(V_G - V_{th})^2$, where W is the channel width (1000 μm), L is the channel length (160 μm), C_i is the gate dielectric layer capacitance per unit area (11.5 nF/cm^2), V_G is the gate voltage, V_{th} is the threshold voltage, and I_{SD} is the source-drain voltage. Devices were measured under nitrogen in a glovebox using a Signatone 1160 probe station and Keithley 4200 semiconductor parametric analyzer. The voltage scan rate of devices was ~15 V/s. Average values were taken from the measurement of at least 4 devices, and error bars were calculated from the standard error of the data set.

High temperature operation: Devices were operated at high temperature on a Heidolph hotplate. Substrates were placed on a machined block of steel with a hole for the temperature probe of the hotplate. The temperature was allowed to equilibrate, and then

devices were placed on the block and allowed to heat up to the temperature of the hotplate. Devices were then measured as stated above under O_2-free conditions. Total measurement time at high temperature was between 30 minutes to an hour.

Details of method used to calculate $\Delta V_T{}^{fb}$: Following device measurement, the device's transfer curve was plotted as a function of $|I_{SD}|^{1/2}$ vs V_G. A voltage range was selected for the forward and reverse scans in such a way as to avoid artifacts that do not represent the semiconductor's intrinsic mobility. Subsequently, the forward and back scan threshold voltages ($V_T{}^f$ and $V_T{}^b$, respectively) were determined by extracting the x-axis intercept of both ranges. Finally, the threshold voltage shift, $\Delta V_T{}^{fb}$, was calculated from the equation $\Delta V_T{}^{fb} = V_T{}^f - V_T{}^b$.

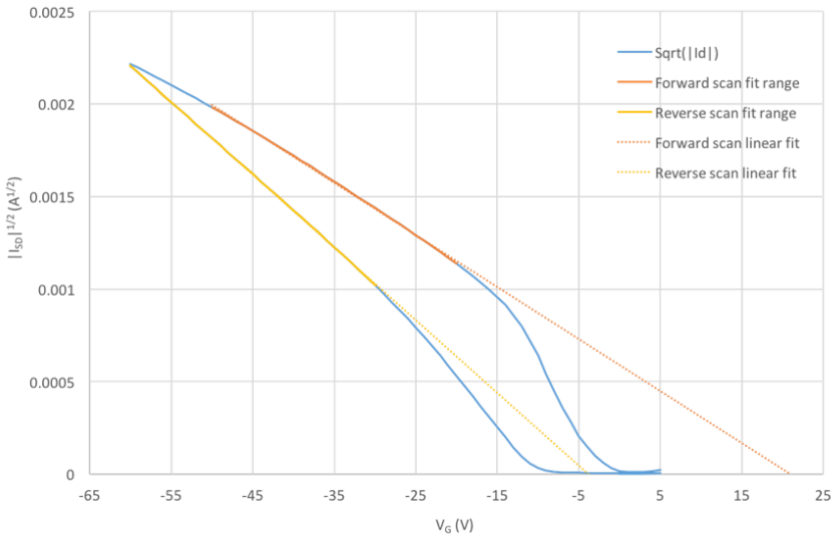

Figure 1-S1. Determination of $\Delta V_T{}^{fb}$ by fitting to the transfer curve.

Device characteristics for varying annealing temperatures: Below are the transfer curves of X2 devices that were annealed at temperatures from 50 ºC to 250 ºC for 10 minutes.

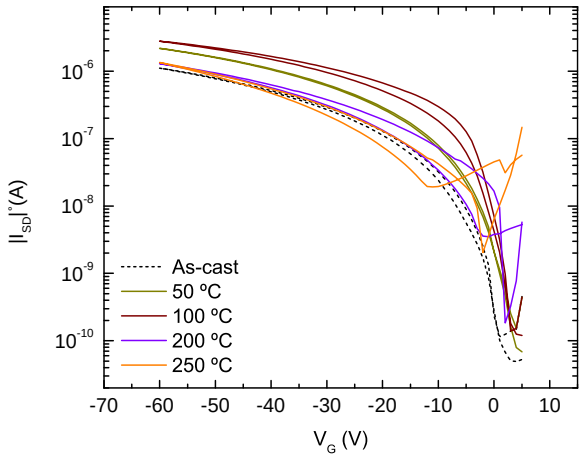

Figure 1-S2. Device characteristics as a function of annealing temperature.

Device characteristics for varying annealing times at 200 ºC: Below are transfer curves of X2 devices that were annealed at 200 ºC for up to one hour.

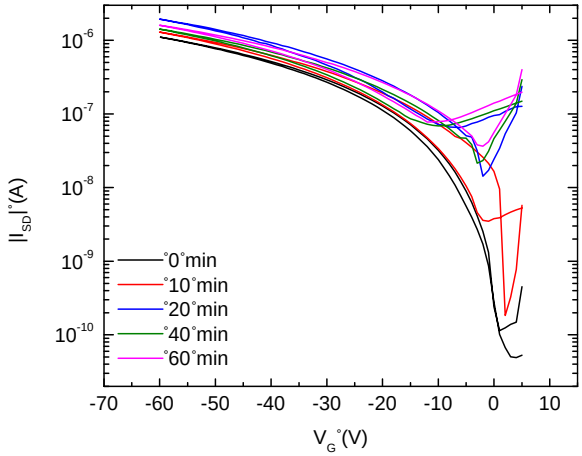

Figure 1-S3. Device characteristics as a function of annealing time at 200 ºC.

Confirmation of ambipolarity

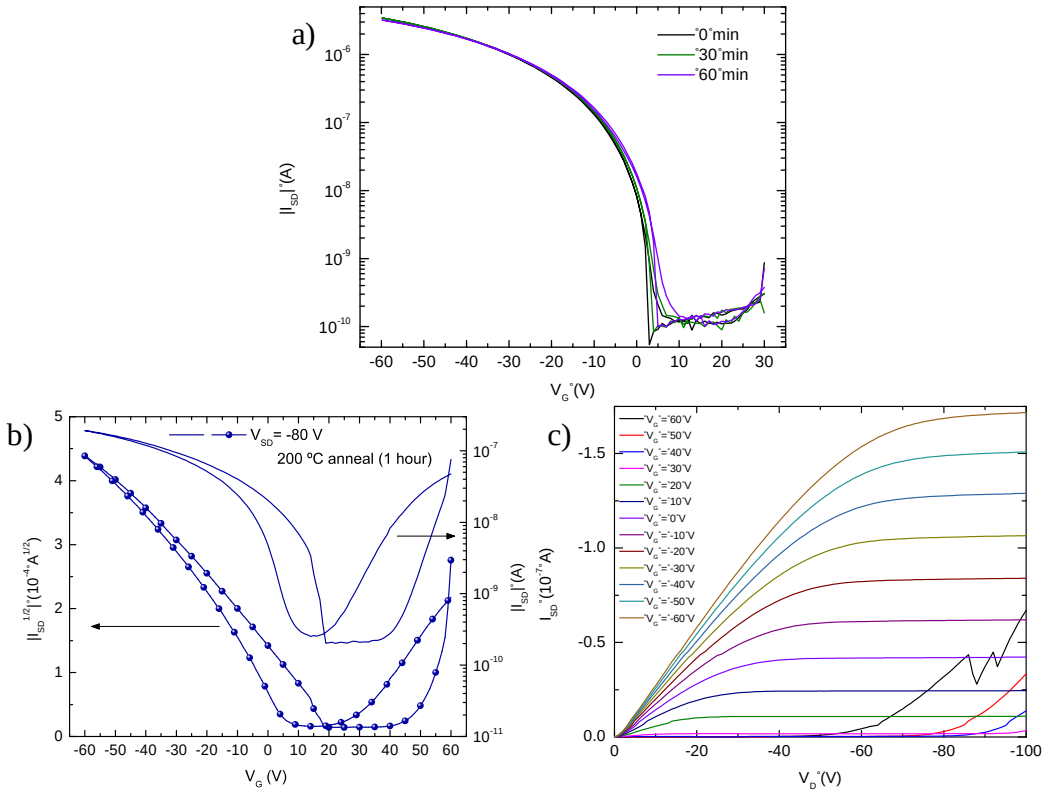

Figure 1-S4. Upon annealing, X2 OFETs show emergent ambipolar charge transport. a) As-cast OFETs remain unipolar p-type devices across multiple measurements and as a function of time. b) Transfer measurement shows the appearance of current at positive V_G. c) Output measurements confirm the appearance of electron injection in annealed X2 OFETs.

Stability of X2 OFETs to multiple high temperature operation cycles

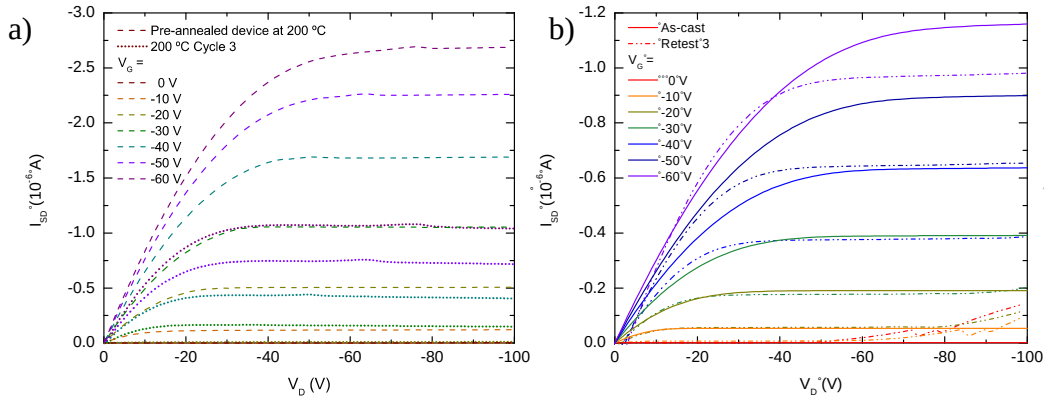

Figure 1-S5. Output measurements confirm the stability of X2 OFETs through three cycles between high (a) and ambient (b) temperature operation. While there are certain changes in the output curves, overall device characteristics are reasonably similar.

Effect of voltage scan rate on device hysteresis: Devices were subjected to the same thermal cycle as those in Figure 1-4 of the main text. Scans were performed at the following rates: slow (~ 1 V/s), normal (~ 15 V/s) and fast (~ 25 V/s). The effective scan rates were achieved by modifying the timing setting of the Keithley 4200 semiconductor parametric analyzer. For "normal" scan rate, settings were untouched. For the "slow" scan rate, a sweep delay time of 1 s was added. For the "fast" scan rate, the settings of the normal scan were modified so that the delay factor was 0.01.

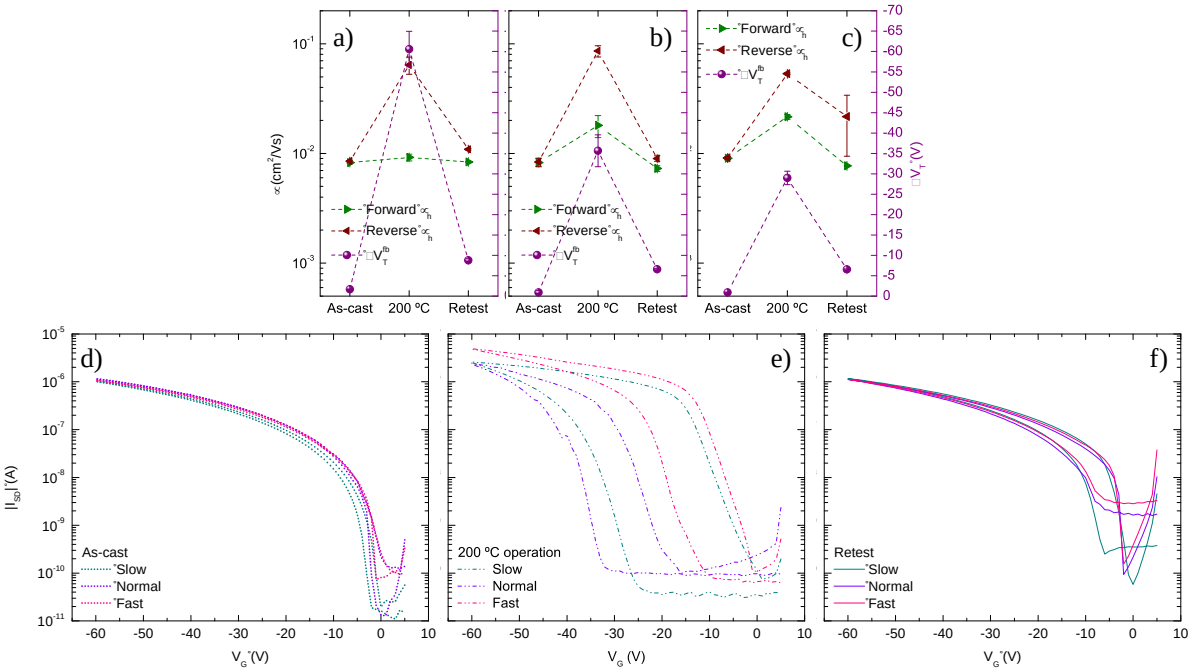

Figure 1-S6. Scan rate dependence of device hysteresis. a-c) Hole mobility and $\Delta V_T{}^{fb}$ characteristics of OFETs through the course of one cycle of operation measured at slow, normal and fast scan rates, respectively. d-f) Representative transfer curves of OFETs measured at three different scan rates in the three parts of the high temperature operation cycle described in the main text. The y axis range is the same for a-c and d-f.

Dependence of hysteresis on scan direction: In order to determine if scan direction has an influence on the transfer characteristics of X2 OFETs, devices were scanned in the normal direction (5 V → -60 V → 5 V) and in the reverse direction (-60 V → 5 V → -60 V).

Despite slight variations, scan direction does not appear to have an influence on the transfer characteristics of the devices.

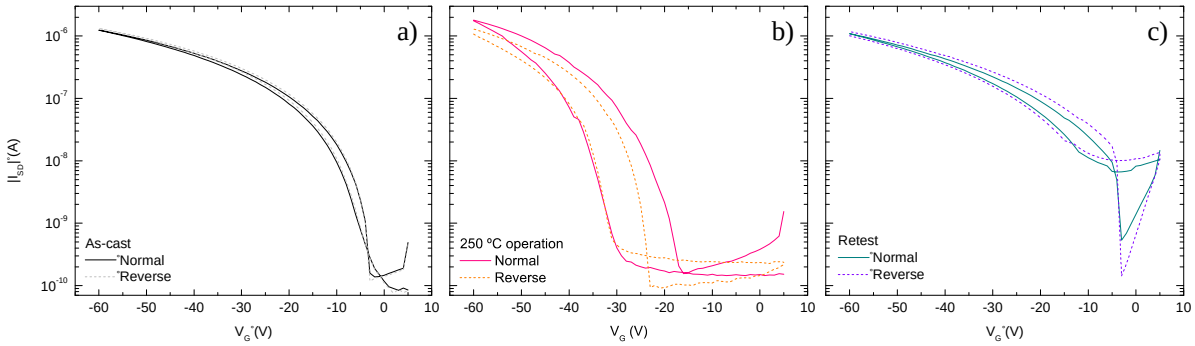

Figure 1-S7. Dependence of hysteresis on scan direction of (a) as-cast devices, (b) devices operated at 250 ºC and (c) devices retested at ambient temperature following operation at 250 ºC. The y axis range is the same for a-c.

Temperature-dependent GIWAXS data: For the high temperature GIWAXS experiments, films were deposited onto bare SiO_2 substrates by the same method as that used for device fabrication. The samples were then put through a heating and cooling cycle, as follows: RT → 50 ºC → 100 ºC → 150 ºC → 200 ºC (and then held for 30 minutes) → 150 ºC → 100 ºC → 50 ºC (end 1st cycle) → 100 ºC → 150 ºC → 200 ºC → RT.

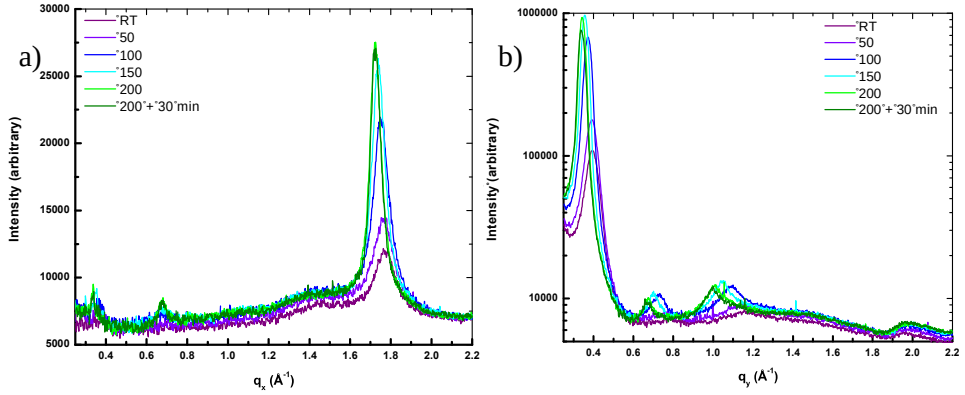

Figure 1-S8. In-plane (a) and out-of-plane (b) line cuts during 1st heating.

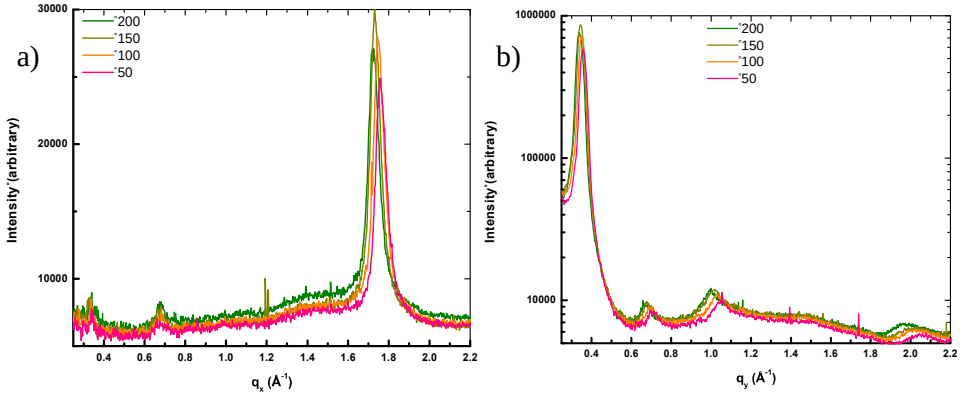

Figure 1-S9. In-plane (a) and out-of-plane (b) line cuts during 1st cooling.

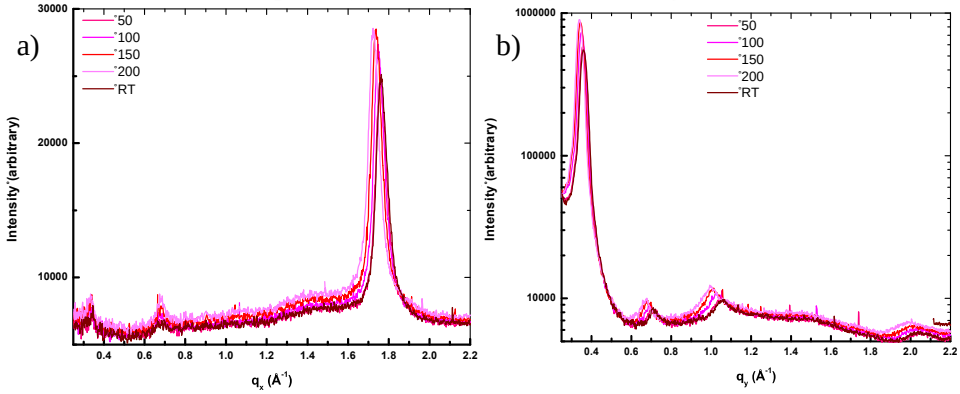

Figure 1-S10. In-plane (a) and out-of-plane (b) line cuts during 2nd heat/cool cycle.

E. References

(1) Kokorowski, S. A.; Olson, G. L.; Roth, J. A.; Hess, L. D. *Phys. Rev. Lett.* **1982**, *48* (7), 498–501.

(2) Martinez, C. R.; Iverson, B. L. *Chem. Sci.* **2012**, *3* (7), 2191.

(3) Kunugi, Y.; Arakawa, T.; Tsutsui, M.; Okamoto, K. *J. Photopolym. Sci. Technol.* **2012**, *25* (3), 285–288.

(4) Podzorov, V. In *Organic Field-Effect Transistors*; Bao, Z., Locklin, J., Eds.; CRC Press: Boca Raton, FL, 2007; pp 27–72.

(5) Pfattner, R.; Mas-Torrent, M.; Bilotti, I.; Brillante, A.; Milita, S.; Liscio, F.; Biscarini, F.; Marszalek, T.; Ulanski, J.; Nosal, A.; Gazicki-Lipman, M.; Leufgen, M.; Schmidt, G.; Laurens, W. M.; Laukhin, V.; Veciana, J.; Rovira, C. *Adv. Mater.* **2010**, *22* (37), 4198–4203.

(6) Chase, D. T.; Fix, A. G.; Kang, S. J.; Rose, B. D.; Weber, C. D.; Zhong, Y.; Zakharov, L. N.; Lonergan, M. C.; Nuckolls, C.; Haley, M. M. *J. Am. Chem. Soc.* **2012**, *134* (25), 10349–10352.

(7) Nalwa, H. S. *Handb. Org. Conduct. Mol. Polym.* **1997**, 87.

(8) Melnyk, A.; Junk, M. J. N.; McGehee, M. D.; Chmelka, B. F.; Hansen, M. R.; Andrienko, D. *J. Phys. Chem. Lett.* **2017**, *8* (17), 4155–4160.

(9) Heumueller, T.; Mateker, W. R.; Sachs-Quintana, I. T.; Vandewal, K.; Bartelt, J. A.; Burke, T. M.; Ameri, T.; Brabec, C. J.; McGehee, M. D. *Energy Environ. Sci.* **2014**, *7* (9), 2974.

(10) Okamoto, T.; Mitsui, C.; Yamagishi, M.; Nakahara, K.; Soeda, J.; Hirose, Y.; Miwa,

K.; Sato, H.; Yamano, A.; Matsushita, T.; Uemura, T.; Takeya, J. *Adv. Mater.* **2013**, *25* (44), 6392–6397.

(11) Li, J.; Bao, Q.; Li, C. M.; Zhang, W.; Gong, C.; Chan-Park, M. B.; Qin, J.; Ong, B. S. *Chem. Mater.* **2010**, *22* (20), 5747–5753.

(12) Cheng, H. H.; Huang, D.-S.; Lin, M.-T. *Microelectron. Reliab.* **2012**, *52* (5), 905–911.

(13) Chung, S.; Lee, J.-H.; Jeong, J.; Kim, J.-J.; Hong, Y. *Appl. Phys. Lett.* **2009**, *94* (25), 253302.

(14) Grimes, R.; Walsh, E.; Walsh, P. *Appl. Therm. Eng.* **2010**, *30* (16), 2363–2369.

(15) Tan, F. L.; Fok, S. C. In *2007 9th Electronics Packaging Technology Conference*; IEEE, 2007; pp 836–842.

(16) Joshi, S.; Pingel, P.; Grigorian, S.; Panzner, T.; Pietsch, U.; Neher, D.; Forster, M.; Scherf, U. *Macromolecules* **2009**, *42* (13), 4651–4660.

(17) Sekitani, T.; Iba, S.; Kato, Y.; Someya, T. *Appl. Phys. Lett.* **2004**, *85* (17), 3902.

(18) Nigam, A.; Kabra, D.; Garg, T.; Premaratne, M.; Rao, V. R. *Org. Electron.* **2015**, *22*, 202–209.

(19) Yi, H. T.; Chen, Z.; Facchetti, A.; Podzorov, V. *Adv. Funct. Mater.* **2016**, *26* (14), 2365–2370.

(20) Letizia, J. A.; Rivnay, J.; Facchetti, A.; Ratner, M. A.; Marks, T. J. *Adv. Funct. Mater.* **2010**, *20* (1), 50–58.

(21) Horowitz, G.; Hajlaoui, M. E.; Hajlaoui, R. *J. Appl. Phys.* **2000**, *87* (9), 4456.

(22) Leufgen, M.; Rost, O.; Gould, C.; Schmidt, G.; Geurts, J.; Molenkamp, L. W.;

Oxtoby, N. S.; Mas-Torrent, M.; Crivillers, N.; Veciana, J.; Rovira, C. *Org. Electron.* **2008**, *9* (6), 1101–1106.

(23) Podzorov, V.; Menard, E.; Borissov, A.; Kiryukhin, V.; Rogers, J. A.; Gershenson, M. E. *Phys. Rev. Lett.* **2004**, *93* (8), 086602.

(24) Tanase, C.; Meijer, E. J.; Blom, P. W. M.; De Leeuw, D. M. *Phys. Rev. Lett.* **2003**, *91* (21), 216601.

(25) Bürgi, L.; Sirringhaus, H.; Friend, R. H. *Appl. Phys. Lett.* **2002**, *80* (16), 2913–2915.

(26) Bürgi, L.; Richards, T. J.; Friend, R. H.; Sirringhaus, H. *J. Appl. Phys.* **2003**, *94* (9), 6129–6137.

(27) Cho, S.; Lee, J. K.; Moon, J. S.; Yuen, J.; Lee, K.; Heeger, A. J. *Org. Electron.* **2008**, *9* (6), 1107–1111.

(28) Chang, S.-W.; Waters, H.; Kettle, J.; Horie, M. *Org. Electron.* **2012**, *13* (12), 2967–2974.

(29) Cho, S.; Seo, J. H.; Kim, G.-H.; Kim, J. Y.; Woo, H. Y. *J. Mater. Chem.* **2012**, *22* (39), 21238.

(30) Horie, M.; Kettle, J.; Yu, C.-Y.; Majewski, L. A.; Chang, S.-W.; Kirkpatrick, J.; Tuladhar, S. M.; Nelson, J.; Saunders, B. R.; Turner, M. L. *J. Mater. Chem.* **2012**, *22* (2), 381–389.

(31) Ford, M. J.; Wang, M.; Patel, S. N.; Phan, H.; Segalman, R. A.; Nguyen, T.-Q.; Bazan, G. C. *Chem. Mater.* **2016**, *28* (5), 1256–1260.

(32) Ford, M. J.; Wang, M.; Phan, H.; Nguyen, T.-Q.; Bazan, G. C. *Adv. Funct. Mater.* **2016**, *26* (25), 4472–4480.

(33) Kyaw, A. K. K.; Lay, L. S.; Peng, G. W.; Changyun, J.; Jie, Z. *Chem. Commun.* **2016**, *52* (2), 358–361.

(34) Lee, B. H.; Hsu, B. B. Y.; Patel, S. N.; Labram, J.; Luo, C.; Bazan, G. C.; Heeger, A. J. *Nano Lett.* **2016**, *16* (1), 314–319.

(35) Liu, X.; Sun, Y.; Perez, L. A.; Wen, W.; Toney, M. F.; Heeger, A. J.; Bazan, G. C. *J. Am. Chem. Soc.* **2012**, *134* (51), 20609–20612.

(36) Liu, X.; Sun, Y.; Hsu, B. B. Y.; Lorbach, A.; Qi, L.; Heeger, A. J.; Bazan, G. C. *J. Am. Chem. Soc.* **2014**, *136* (15), 5697–5708.

(37) Liu, X.; Burgers, M. A.; Hsu, B. B. Y.; Coughlin, J. E.; Perez, L. A.; Heeger, A. J.; Bazan, G. C. *RSC Adv.* **2015**, *5* (108), 89144–89148.

(38) Petit, C.; Zander, D.; Lmimouni, K.; Ternisien, M.; Tondelier, D.; Lenfant, S.; Vuillaume, D. *Org. Electron.* **2008**, *9* (6), 979–984.

(39) Padma, N.; Sawant, S. N.; Sudarsan, V.; Sen, S.; Gupta, S. K. *Phys. status solidi* **2013**, *210* (10), 2111–2120.

(40) Padma, N.; Sawant, S. N.; Sen, S. *Mater. Sci. Semicond. Process.* **2015**, *30*, 18–24.

(41) Sachtler, W. M. H.; Dorgelo, G. J. H.; Holscher, A. A. *Surf. Sci.* **1966**, *5* (2), 221–229.

(42) Brown, A. R.; Jarrett, C. P.; de Leeuw, D. M.; Matters, M. *Synth. Met.* **1997**, *88* (1), 37–55.

(43) Horowitz, G. *Adv. Mater.* **1998**, *10* (5), 365–377.

(44) Coropceanu, V.; Cornil, J.; da Silva Filho, D. A.; Olivier, Y.; Silbey, R.; Brédas, J.-L. *Chem. Rev.* **2007**, *107* (4), 926–952.

(45) Choi, S. H.; Risko, C.; Delgado, M. C. R.; Kim, B.; Brédas, J.-L.; Frisbie, C. D. *J. Am. Chem. Soc.* **2010**, *132* (12), 4358–4368.

(46) DeLongchamp, D. M.; Kline, R. J.; Fischer, D. A.; Richter, L. J.; Toney, M. F. *Adv. Mater.* **2011**, *23* (3), 319–337.

(47) Egginger, M.; Bauer, S.; Schwödiauer, R.; Neugebauer, H.; Sariciftci, N. S. *Monatshefte für Chemie - Chem. Mon.* **2009**, *140* (7), 735–750.

(48) Choi, H. H.; Baek, J. Y.; Song, E.; Kang, B.; Cho, K.; Kwon, S.-K.; Kim, Y.-H. *Adv. Mater.* **2015**, *27* (24), 3626–3631.

(49) Okachi, T.; Kashiki, T.; Ohya, K. *Proc. SPIE* **2015**, *9568*, 95680I.

(50) Yun, H.-J.; Lee, G. B.; Chung, D. S.; Kim, Y.-H.; Kwon, S.-K. *Adv. Mater.* **2014**, *26* (38), 6612–6616.

(51) Han, A.-R.; Dutta, G. K.; Lee, J.; Lee, H. R.; Lee, S. M.; Ahn, H.; Shin, T. J.; Oh, J. H.; Yang, C. *Adv. Funct. Mater.* **2015**, *25* (2), 247–254.

(52) Zhang, X.-H.; Domercq, B.; Kippelen, B. *Appl. Phys. Lett.* **2007**, *91* (9), 092114.

(53) Zhao, Y.; Guo, Y.; Liu, Y. *Adv. Mater.* **2013**, *25* (38), 5372–5391.

(54) Phan, H.; Wang, M.; Bazan, G. C.; Nguyen, T.-Q. *Adv. Mater.* **2015**, *27* (43), 7004–7009.

II. Orientational Preferences are the Result of a Kinetic Trap

A. Molecular orientation with respect to the substrate

The orientation of molecular organic semiconducting materials is important due to the anisotropic nature of charge transport through π-π stacking, which can impact device performance. For applications such as organic field-effect transistors (OFETs), edge-on orientation relative to the substrate may be preferable.[1,2] However, for applications in which charges move in the direction normal to the substrate surface (e.g. diodes, OLEDs, OPV) it is beneficial for the materials to orient face-on, as the π-π stacking is in the direction of charge transport.[3–5] However, orientation with respect to the substrate is not the single determining factor of charge carrier mobility in a given direction.[6–10] Factors such as crystal structure, formation of connected networks, grain boundaries and intermolecular electronic coupling play a role, as well.[11] Even though the degree by which orientation impacts charge carrier mobility is under examination, the forces and molecular features that impact the preferred orientation have not been fully elucidated.

Previous reports[12] demonstrated that material orientation relative to the substrate can be controlled by processing conditions. For the small molecule donor *p*-SIDT(FBTTh$_2$)$_2$, spin coating the material with or without the solvent additive diiodooctane results in face-on or edge-on crystallites of the donor, respectively. In bilayer devices, improved performance is due to an increase in open circuit voltage from 0.69 V to 0.84 V, attributed to improved π orbital overlap with the acceptor, PCBM. The widely studied polymer N2200 has also been shown to change orientation following annealing above its melting point.[13] In the as-cast

film, N2200 crystallites orient face-on and flip to edge-on when melt-annealed. There have been several examples of this behavior in the literature,[14–16] but no unifying mechanism exists so far. Other reports[17,18] in which poly(3-alkylthiophene) polymers were studied suggest that higher crystallinity and pre-aggregation in solution favor the edge-on orientation; however, no chemical explanation for this phenomenon is given.

In summary, it is understood that orientation of a material can be controlled by processing conditions, yet there is no explanation for the relationship between chemical structure and the final organization obtained from solution. Given the absence of modelling tools, *a priori* knowledge or other approaches that allow one to predict molecular orientation, this question remains open to investigation.

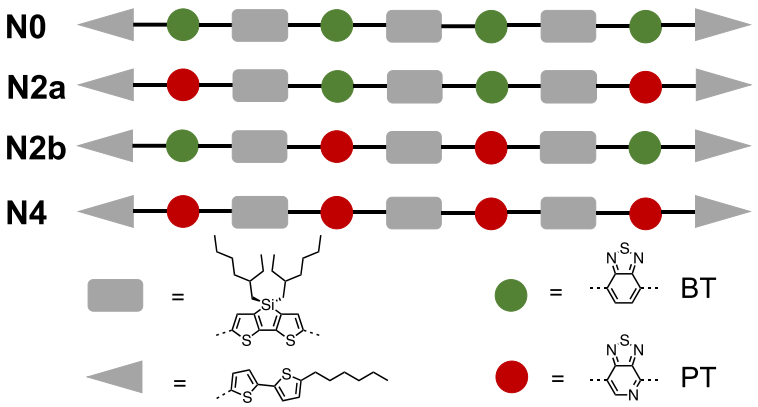

Scheme 2-1. Chemical structures of the N series molecules. From top to bottom: N0, N2a, N2b, N4.

It has been previously reported[19] that four isomorphic organic semi-conductors, Scheme 2-1 (full chemical structures in Scheme 2-S1), whose crystallite orientation in the as-cast film depends on the position of the pyridylthiadiazole (PT) acceptor fragment within the conjugated backbone. It was found that the molecules with benzothiadiazole (BT) acceptors

in the inner positions assume an edge-on orientation, while those with PT units at the same positions show face-on orientation. The difference in crystallite orientation, especially in the isomers N2a and N2b, raises the question of the origin of this phenomenon.

It is important to consider that the differences in orientation arise from very small (single atom) changes in chemical structure. Are the face-on crystallites the thermodynamically preferred orientation, or is it a case of kinetic trapping?[20–23] This question is relevant due to the impact of crystallite orientation on the preferred direction of charge transport in the solid state, especially since a molecule in this group has been shown to be able to withstand significant thermal stress in an organic field effect transistor (OFET) device architecture.[24] While previous studies relied on processing conditions to modify crystallite orientation, I present in this chapter a system in which this determination is made based on chemical structure.

Using grazing incidence wide-angle X-ray scattering (GIWAXS), and by in-situ melt annealing of films of these four isomorphic organic semiconductors, I sought to obtain insight into the kinetic and thermodynamic crystallite orientations of these materials.

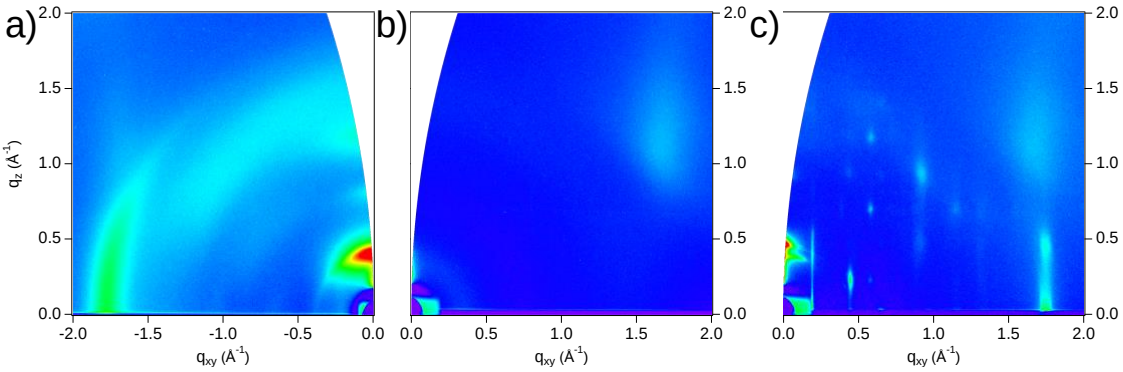

Figure 2-1. GIWAXS diffraction patterns of N0 as-cast (a), in the melt (b) at 250 ºC and melt-cooled (c).

B. Results and discussion

Figure 2-1 illustrates the diffraction patterns obtained for a film of N0. Figure 2-1a is the diffraction pattern of the as-cast N0 film. The two most distinct peaks are the lamellar stacking peak (~ 0.4 $Å^{-1}$ along the q_z axis) and the π-π stacking peak (~ 1.8 $Å^{-1}$ along the q_{xy} axis), while the off-axis area of the image contains diffuse scattering. Overtones of the lamellar stacking peak are visible along the q_z axis. As is typical of a spin-coated film, the diffraction peaks show some dependence of intensity with respect to the azimuthal angle, χ, indicating that the crystallite orientation is not perfectly uniform.[25] Film heating was achieved *via* a temperature-controlled stage. Steps of 50 ºC to 25 ºC were taken below 200 ºC. Smaller increases in temperature of ~ 10 ºC were effected as the films neared the melting point, as determined by differential scanning calorimetry (DSC).[19,26] The temperatures at which scattering peaks disappear roughly matches the melting points from DSC (258 ºC, 269 ºC, 259 ºC and 265 ºC for N0, N2a, N2b and N4, respectively), as seen in Figure 2-S1. Diffraction from the fully amorphous melt is characterized by the lack of any discernable peaks (Figure 2-1b). The broad peak at [1.7,1.2], seen in other images as well, is due to diffraction from the underlying Si substrate. Finally, Figure 2-1c is the diffraction pattern of the N0 film following cooling from the melt (melt annealing). The stacking distances corresponding to the peaks discussed earlier have not changed significantly. The π-π stacking distance remains at 3.6 Å, and the lamellar stacking distance changes from 15.5 Å to 16.0 Å, possibly due to unfolding of the alkyl chains or a change of inclination of the

molecules relative to the substrate normal.[27] Compared to Figure 2-1a, the diffraction pattern of Figure 2-1c indicates a higher degree of order within the crystallites or throughout the film. For instance, the full width half-maximum (FWHM) of the lamellar and π-π stacking peaks change from 0.06 $Å^{-1}$ to 0.03 $Å^{-1}$ and 0.12 $Å^{-1}$ to 0.07 $Å^{-1}$, respectively. This corresponds to a change in the crystalline correlation length (L_C)[28] from 95 Å to 171 Å for the lamellar stacking peak and 47 Å to 82 Å for the π-π stacking peak. It is unclear whether this increase in the L_C is due purely to improved order within the crystallites, or to larger crystallites as well. There is also less intensity dependence with respect to χ, indicating that the orientation of the crystallites has become more uniformly edge-on. After melt-annealing, the off-axis area displays distinct peaks, attributed to improved order within the crystallites, likely due to the extra thermal energy and crystallization time afforded by melt-annealing the film. There is also a new peak at 0.5 $Å^{-1}$ along the q_z axis, which is indicative of a secondary lamellar stacking distance of 13.7 Å. The new off-axis π-π stacking peak at [1.7,0.4] (q = 1.8 $Å^{-1}$, corresponding to ~ 3.5 Å) suggests that there may be two coexisting polymorphs, supported by the presence of multiple endotherms in the DSC heating traces[19] and a second lamellar stacking peak. However, without the crystal structure, it is difficult to attribute these new peaks to any specific interactions or changes in local packing.

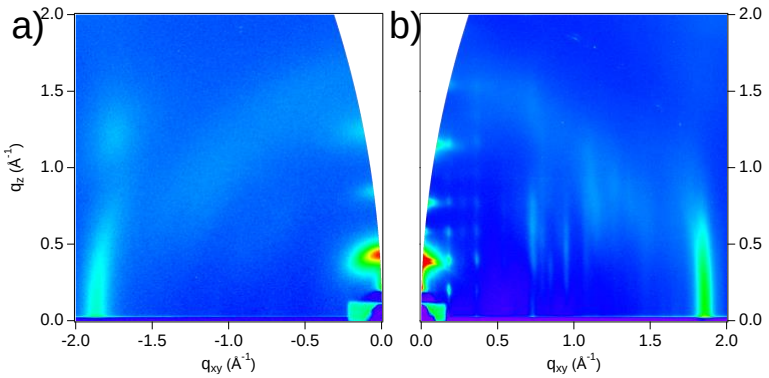

Figure 2-2. GIWAXS diffraction patterns of N2a as-cast (a) and melt-cooled (b).

Similar observations can be made for films of N2a. Figure 2-2a shows the diffraction pattern of the as-cast N2a film. The lamellar stacking peak is at 0.4 Å^{-1} along the q_z axis, along with its overtones, and the π-π stacking peak is located at 1.8 Å^{-1} along the q_{xy} axis. Some diffuse scattering is also visible in the off-axis area. The melt diffraction pattern of the N2a film is not shown as it is the same as that of the N0 film (i.e. no visible scattering peaks). The lamellar stacking distance in the melt-cooled film (Figure 2-2b) increases from 14.6 Å to 16.3 Å, and the π–π stacking distance does not change from 3.4 Å. As with the melt-annealed N0 films, the L_C increases from 97 Å to 182 Å for the lamellar stacking and 67 Å to 109 Å for the π-π stacking. There is also less disorder along χ, indicating more uniform orientation of the crystallites relative to the substrate. The diffraction pattern of the melt-annealed N2a film also shows the appearance of two groups of off-axis peaks. The first group of peaks (q_{xy} < 0.5 Å^{-1}) is well-defined along the q_z and q_{xy} axes and has multiple overtones. This indicates that the reflections of the unit cell responsible for this diffraction have a low degree of disorder. The second group of off-axis peaks (0.5 Å^{-1} < q_{xy} < 1.5 Å^{-1}) is

well-defined in the q_{xy} plane, but appears poorly defined in the q_z direction, indicating a higher degree of stacking disorder in the out-of-plane direction.

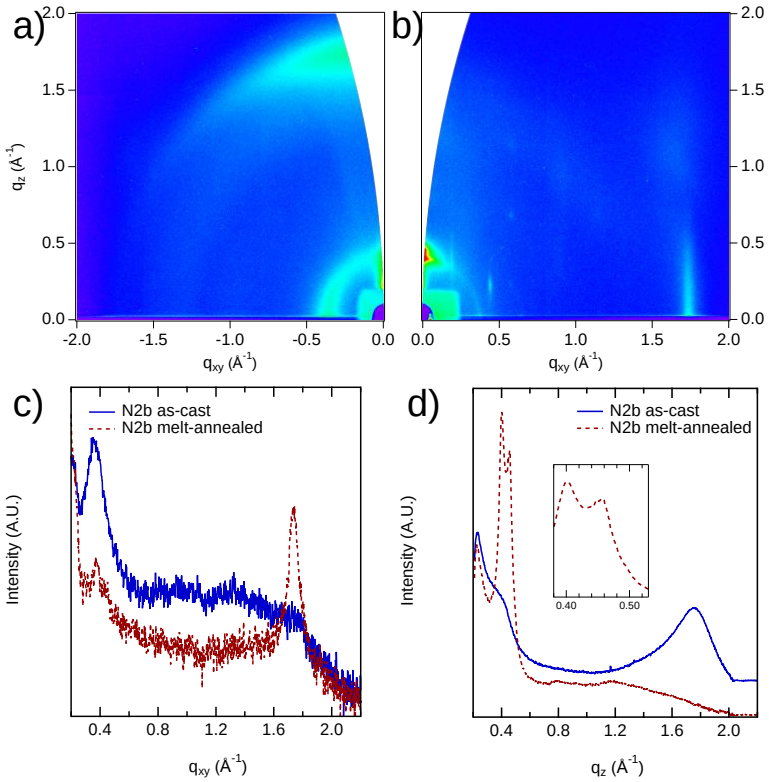

Figure 2-3. GIWAXS diffraction patterns of N2b as-cast (a) and melt-cooled (b). Plots show in-plane (c) and out-of-plane (d) line cuts of N2b as-cast and melt-cooled. The inset in (d) highlights the two lamellar stacking peaks of the melt-annealed film.

As previously discussed in the introduction, the as-cast diffraction pattern of the N2b film (Figure 2-3a) is noticeably different from those of the previously discussed materials, N0 and N2a. The face-on orientation of as-cast N2b crystallites is consistent with previously reported data.[19] The line cuts in Figure 2-3 show that, following melt-annealing, the lamellar and π-π stacking peaks have shifted by 90º so that the π-π stacking peak is located along the q_z axis, while the lamellar stacking peak is located on the q_{xy} axis. Although the axes along

which the stacking peaks appear have changed, their q values have not. The π-π stacking peak is at 1.8 $Å^{-1}$ and the lamellar stacking peak is at 0.4 $Å^{-1}$. The diffraction peaks from the as-cast N2b film are relatively broad and show some dependence of intensity with respect to χ. Following melt-annealing, the new edge-on crystallite peaks are located at 1.7 $Å^{-1}$ along the q_{xy} axis (π-π stacking) and 0.4 $Å^{-1}$ along the q_z axis (lamellar stacking). As with N0 (Figure 2-S2), there is also a new lamellar stacking peak that appears at 0.5 $Å^{-1}$ along the q_z axis. Similarly to the previous materials, the π-π stacking distances do not change significantly, increasing from 3.6 Å to 3.7 Å, while the lamellar stacking distance decreases slightly from 17.6 Å to 15.7 Å. The new lamellar stacking distance (13.8 Å) is also consistent with that of N0 (13.7 Å). As observed with the other melt-annealed samples, the degree of disorder decreases compared to the as-cast films. The L_C for the π-π and lamellar stacking peaks increase from 24 Å to 94 Å and from 36 Å to 175 Å, respectively. Off-axis peaks also appear following melt-annealing, indicating improved intra-crystalline order. Melt-annealing of the molecule N2b, which has interior PT acceptor fragments, therefore produces a drastic change in the diffraction pattern of the film. The main diffraction peaks reorient and resemble the melt-annealed diffraction patterns of N0 and N2a.

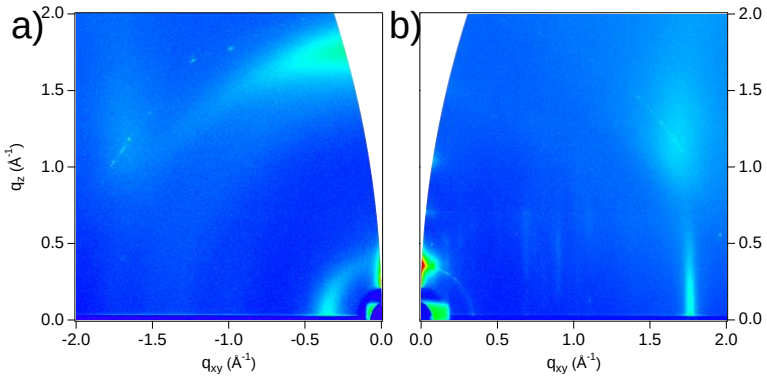

Figure 2-4. GIWAXS diffraction patterns of N4, as-cast (a) and melt-cooled (b).

N4 exhibits the same behavior as N2b, both in the as-cast film and following melt-annealing. In the as-cast diffraction pattern (Figure 2-4a), the π-π stacking peak is located at 1.8 $Å^{-1}$ along the q_z axis and the lamellar stacking peak is located at 0.4 $Å^{-1}$ along the q_{xy} axis. Both peaks appear broad and show intensity dependence with χ, indicating some disorder in the crystallite orientation. Following melt-annealing (Figure 2-4b), the crystallite orientation flips from face-on to edge-on. The π-π stacking diffraction peak is now located at 1.7 $Å^{-1}$ along the q_{xy} axis and the lamellar stacking peak is located at 0.4 $Å^{-1}$ along the q_z axis. Stacking distances do not change significantly. There is no change in the π-π stacking distance, and the lamellar stacking distance decreases from 17.9 Å to 17.7 Å. The L_C increase from 26 Å to 122 Å for π-π stacking and from 34 Å to 131 Å for lamellar stacking. A secondary, much less intense, lamellar stacking peak is observed at 0.40 $Å^{-1}$ along the q_z axis, corresponding to a stacking distance of 15.8 Å. As observed in the previous examples, the azimuthal dependence of the peaks decreases significantly, indicating more uniform crystallite orientation with respect to the substrate. Off-axis peaks also start to appear, though they are not sharp or intense enough to characterize. This suggests that the degree of ordering is improved as compared to the as-cast film, but not to the same extent as in the other materials.

The reorientation of N2b and N4 crystallites following melt-annealing of the films indicates that the initial (as-cast) face-on crystallite orientation is kinetically trapped. In the as-cast films, the relative population of edge-on to face-on crystallites of N2a and N2b is

very high, while the relative population of face-on to edge-on crystallites is significantly smaller (Figure 2-S3 and Table 2-S1). The lower relative population of face-on crystallites in the as-cast N2b and N4 films suggests that the face-on orientation is not as favorable as the edge-on crystallites in the as-cast N0 and N2a films. Following melt-annealing, the relative population of edge-on to face-on crystallites is at least 8:1 in all four films, indicating that crystallites of all four materials significantly prefer the edge-on orientation. While the mechanism for kinetic trapping into face-on orientation of crystallites is not yet completely understood (see relevant system in N2200)[13–16], the possibility of there being a kinetic trap during spin coating is not out of the question. When comparing the lattice parameters of the sets of materials (kinetically trapped and edge-on) in Table 2-1, it is important to note that there are some consistent trends which could correlate to the observed behavior. Following melt-annealing, the (primary) lamellar stacking distances of all the materials converge to approximately 16 Å. This suggests that the thermodynamically preferred lamellar stacking distance of all four materials does not vary significantly. However, the as-cast lamellar stacking distances are different. The lamellar stacking distances of as-cast N0 and N2a lattices are slightly shorter than the equilibrium distance: 15.5 Å and 14.6 Å, respectively. On the other hand, the lamellar stacking distances of the lattices of as-cast N2b and N4 films are almost 2 Å longer: 17.6 Å and 17.9 Å, respectively. The L_C of the as-cast N0 and N2a crystallites are also approximately twice as large as those of the as-cast N2b and N4 crystallites, which suggests that there is a larger degree of disorder in the latter. These differences indicate that face-on orientation may be a quenched metastable state. The degree of variation in the π-π stacking distance is very small: a range of only 0.3 Å (approximately

2%). This is likely due to the relatively stronger π-π interactions and the structural similarity of the four conjugated backbones.

Diffraction peak		As-cast		Melt-annealed		% Change	
		d spacing (Å)	L_C (Å)	d spacing (Å)	L_C (Å)	d spacing	L_C
N0	Lamellar	15.5	95.0	16.0	171.3	3.7	80.4
	Lamellar 2			13.7	336.2		
	π-π	3.6	46.5	3.6	81.7	1.8	75.8
	π-π 2			3.5	48.2		
N2a	Lamellar	14.6	96.7	16.3	182.0	11.6	88.2
	Lamellar 2						
	π-π	3.4	67.6	3.4	109.4	0.3	61.9
N2b	Lamellar	17.6	36.4	15.7	174.8	-11.1	380.2
	Lamellar 2			13.8	95.0		
	π-π	3.6	24.0	3.7	93.5	1.8	288.9
N4	Lamellar	17.9	34.6	17.7	130.8	-1.2	278.2
	Lamellar 2			15.8	77.6		
	π-π	3.6	26.1	3.6	122.1	1.6	367.8

Table 2-1. Spacing distances and L_C derived from GIWAXS diffraction peaks.

C. Conclusions

In conclusion, I have shown that even though the four N series molecules have different orientational preferences relative to the substrate when kinetically trapped during spin coating, their thermodynamically preferred orientation is the same. As demonstrated by *in-situ* GIWAXS measurements, the molecules with inner BT units (N0 and N2a) are able to achieve the thermodynamically preferred orientation during spin coating. However, the molecules with inner PT acceptor units (N2b and N4) are kinetically trapped in the face-on

orientation during spin coating. After annealing these films to the melt and then cooling, the resulting crystallites are oriented edge-on relative to the substrate. While there is not yet a mechanistic explanation for the kinetically determined orientational preferences observed in these organic semiconductors, it is worth noting that crystallite orientation has been shown to depend on processing conditions. This chapter shows such changes within a series of closely chemically related materials, especially for two isomers: N2a and N2b. Furthermore, the N series of molecular semiconductors presents a well-defined, monodisperse system to study crystallite reorientation that has previously been observed in polydisperse systems. An understanding of the degree to which organizational preferences under kinetic control can be pre-programmed through the chemical structure of molecular semiconductors remains a formidable challenge. However, it is worth re-emphasizing that such control would open opportunities to optimize the charge carrier transport in the bulk and thereby relevant electronic device properties.

The dynamic behavior presented in this study, as well as in previous reports for both molecular and polymeric organic semiconductors has the potential to be both a way to control for the solid-state organization of organic semiconductors, as well as a source of significant instability. Further understanding of the mechanism of kinetic trapping during film formation is necessary. It is also important to highlight that most studies of thin-film morphology at the molecular level, including this one, rely upon diffraction methods such as GIWAXS or transmission electron microscopy to probe the material. However, it is well understood that a significant portion of OSC thin films and solids is composed of amorphous regions which are inaccessible by diffraction techniques. For this reason, a method that can

probe the entirety of the solid is necessary. I will discuss such a method in the following chapter.

D. Experimental and Supplementary Information

Silicon substrates (with native oxide) were cleaned by sonication in piranha solution (3:1 H_2SO_4:H_2O_2), acetone and isopropanol for approximately 5 minutes each. The substrates were subsequently dried in an oven at 130 ºC and cleaned via UV-ozone treatment for 30 minutes each. The substrates were then brought into a glovebox under N_2 atmosphere, where the films were deposited via spin coating at 1500 rpm for 60 s from chloroform solutions (10 mg/mL) of each material.

GIWAXS measurements were taken at beamline 11-3 of the Stanford Synchrotron Radiation Lightsource (SSRL) using a CCD detector with a beam energy of 12.4 keV. The films were melt annealed by heating the stage above the melting point of the material (confirmed by no X-ray diffraction) and then allowing it to cool back down to ambient temperature.

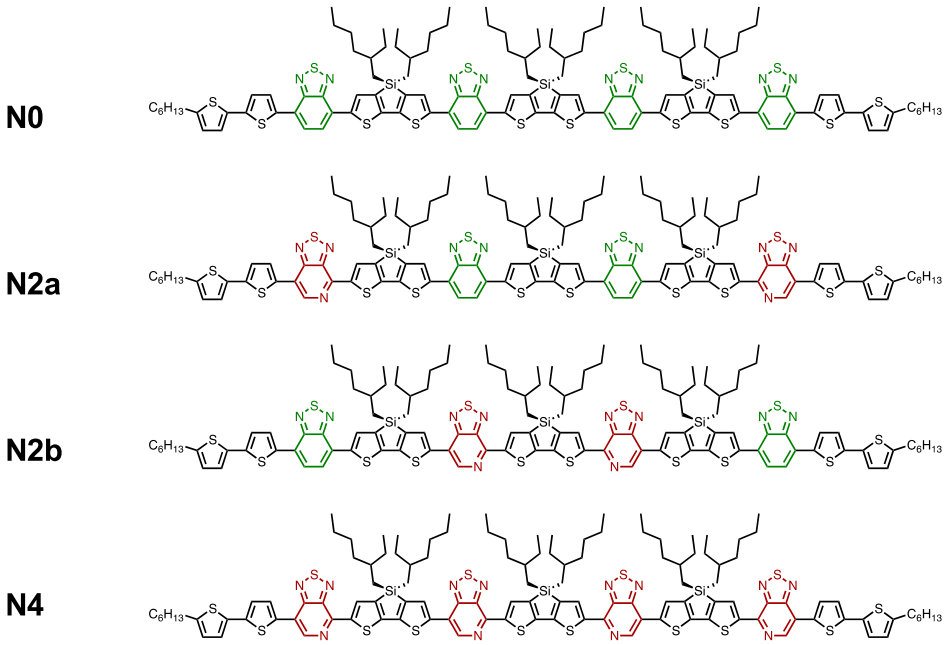

Scheme 2-S1. Full chemical structures of (from top to bottom) N0, N2a, N2b, N4.

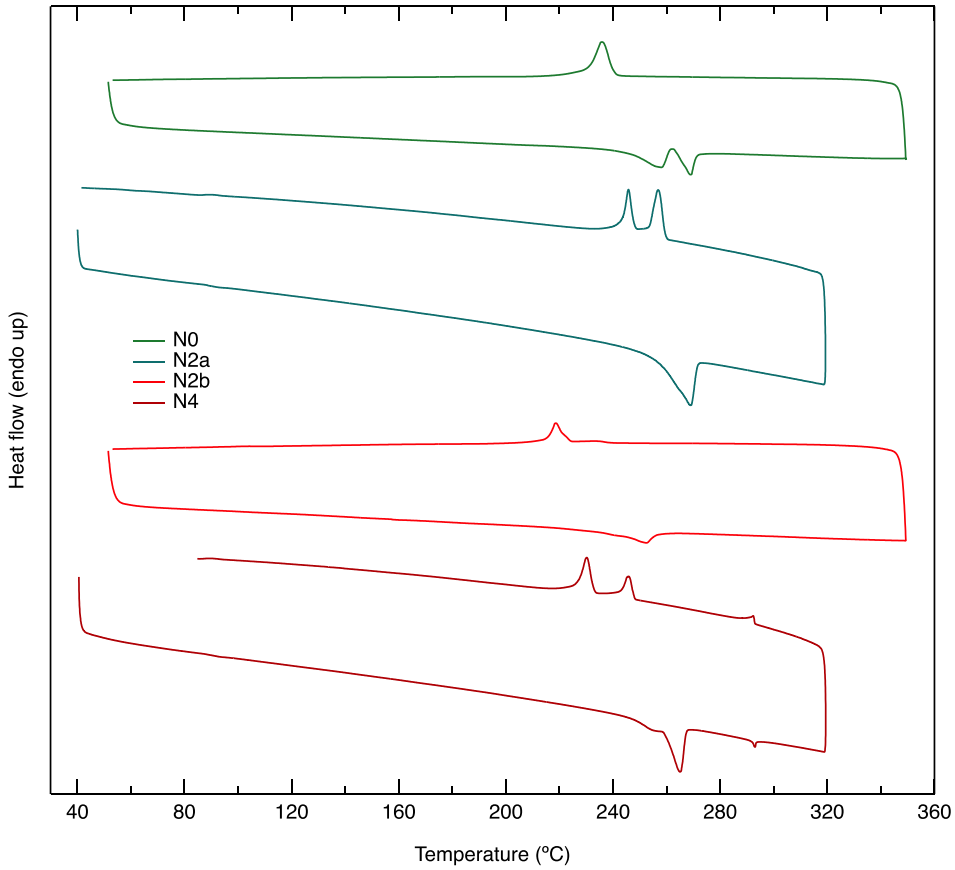

Figure 2-S1. DSC traces of N0, N2a, N2b and N4, taken from references 19 and 26 in the main text.

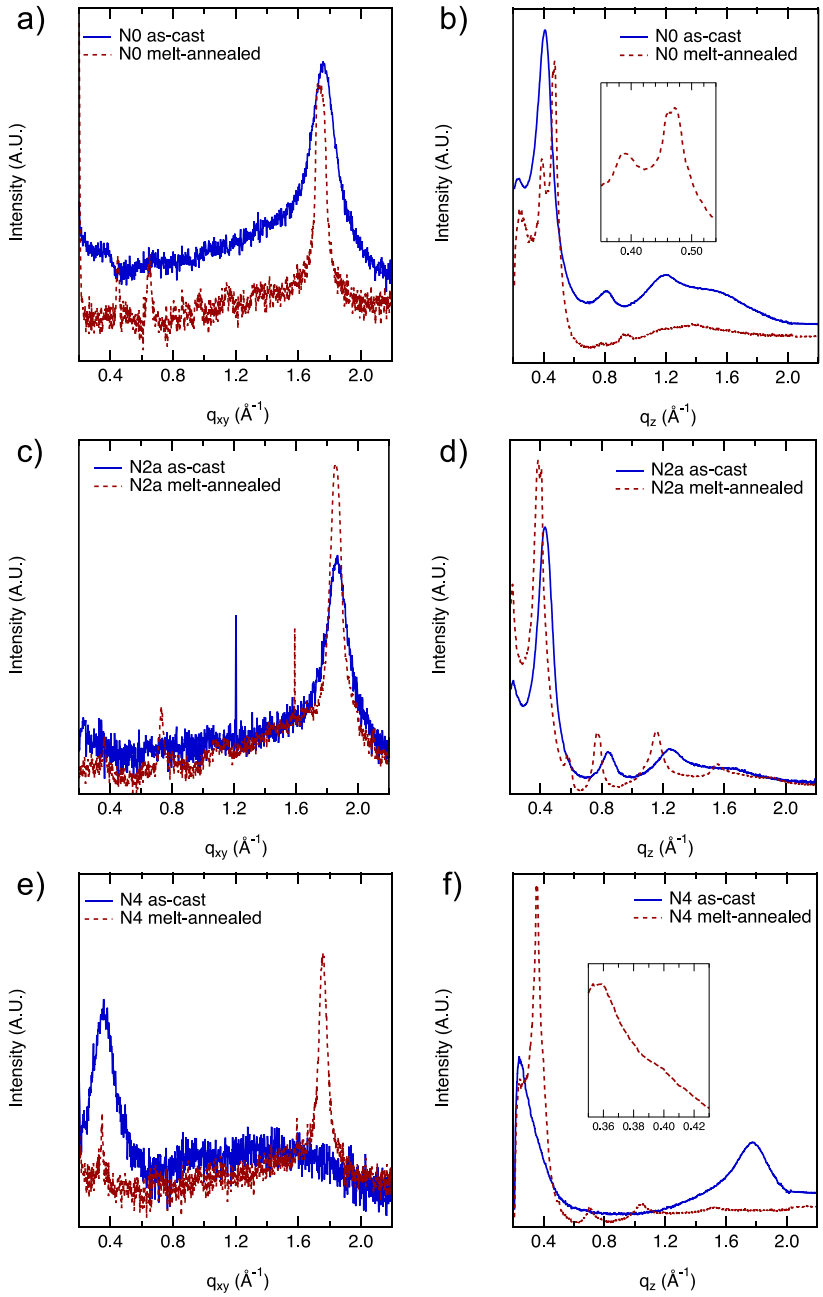

Figure 2-S2. In-plane (a,c,e) and out-of-plane (b,d,f) line cuts of N0, N2a and N4, respectively. As noted in the main text and confirmed by the line cuts, only the N4 crystallites flip from face-on to edge-on following melt-annealing. Insets highlight the two lamellar stacking peaks of the melt-annealed films.

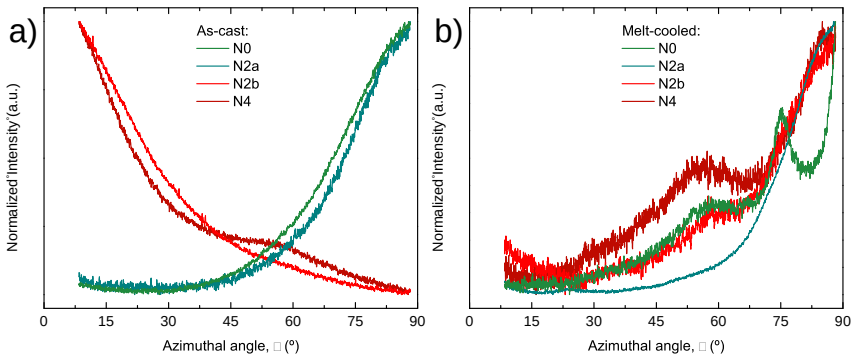

Figure 2-S3. Distribution of the π-π stacking peak intensity in the as-cast (a) and melt-cooled (b) film diffraction spectra.

Material	As-cast	Melt-cooled
N0	40:1	12:1
N2a	32:1	54:1
N2b	1:2.5	12:1
N4	1:1.5	8:1

Table 2-S1. Ratio of edge-on:face-on crystallites in the as-cast and melt-cooled films.

E. References

(1) Chen, H.; Guo, Y.; Yu, G.; Zhao, Y.; Zhang, J.; Gao, D.; Liu, H.; Liu, Y. Highly π-Extended Copolymers with Diketopyrrolopyrrole Moieties for High-Performance Field-Effect Transistors. *Adv. Mater.* **2012**, *24* (34), 4618–4622.

(2) Chen, Z.; Lee, M. J.; Shahid Ashraf, R.; Gu, Y.; Albert-Seifried, S.; Meedom Nielsen, M.; Schroeder, B.; Anthopoulos, T. D.; Heeney, M.; McCulloch, I.; Sirringhaus, H. High-Performance Ambipolar Diketopyrrolopyrrole-Thieno[3,2- b]Thiophene Copolymer Field-Effect Transistors with Balanced Hole and Electron Mobilities. *Adv. Mater.* **2012**, *24* (5), 647–652.

(3) Tumbleston, J. R.; Collins, B. A.; Yang, L.; Stuart, A. C.; Gann, E.; Ma, W.; You, W.; Ade, H. The Influence of Molecular Orientation on Organic Bulk Heterojunction Solar Cells. *Nat. Photonics* **2014**, *8* (5), 385–391.

(4) Chen, W.; Xu, T.; He, F.; Wang, W.; Wang, C.; Strzalka, J.; Liu, Y.; Wen, J.; Miller, D. J.; Chen, J.; Hong, K.; Yu, L.; Darling, S. B. Hierarchical Nanomorphologies Promote Exciton Dissociation in Polymer/Fullerene Bulk Heterojunction Solar Cells. *Nano Lett.* **2011**, *11* (9), 3707–3713.

(5) Kim, D. H.; Ayzner, A. L.; Appleton, A. L.; Schmidt, K.; Mei, J.; Toney, M. F.; Bao, Z. Comparison of the Photovoltaic Characteristics and Nanostructure of Fullerenes Blended with Conjugated Polymers with Siloxane-Terminated and Branched Aliphatic Side Chains. *Chem. Mater.* **2013**, *25* (3), 431–440.

(6) Kim, Y.; Long, D. X.; Lee, J.; Kim, G.; Shin, T. J.; Nam, K. W.; Noh, Y. Y.; Yang, C. A Balanced Face-On to Edge-On Texture Ratio in Naphthalene Diimide-Based Polymers with Hybrid Siloxane Chains Directs Highly Efficient Electron Transport. *Macromolecules* **2015**, *48* (15), 5179–5187.

(7) Pei, M.; Park, K. H.; Jang, M.; Lee, S. B.; Ahn, J.; Kim, Y.-H.; Yang, H. Control of Consistent Ordering in π-Conjugated Polymer Films for Organic Field-Effect Transistor Applications. *RSC Adv.* **2016**, *6* (75), 70733–70739.

(8) Kronemeijer, A. J.; Gili, E.; Shahid, M.; Rivnay, J.; Salleo, A.; Heeney, M.; Sirringhaus, H. A Selenophene-Based Low-Bandgap Donor-Acceptor Polymer Leading to Fast Ambipolar Logic. *Adv. Mater.* **2012**, *24* (12), 1558–1565.

(9) Zhang, X.; Richter, L. J.; Delongchamp, D. M.; Kline, R. J.; Hammond, M. R.; McCulloch, I.; Heeney, M.; Ashraf, R. S.; Smith, J. N.; Anthopoulos, T. D.; Schroeder, B.; Geerts, Y. H.; Fischer, D. A.; Toney, M. F. Molecular Packing of High-Mobility Diketo Pyrrolo-Pyrrole Polymer Semiconductors with Branched Alkyl Side Chains. *J. Am. Chem. Soc.* **2011**, *133* (38), 15073–15084.

(10) Rivnay, J.; Toney, M. F.; Zheng, Y.; Kauvar, I. V.; Chen, Z.; Wagner, V.; Facchetti, A.; Salleo, A. Unconventional Face-on Texture and Exceptional in-Plane Order of a High Mobility n-Type Polymer. *Adv. Mater.* **2010**, *22* (39), 4359–4363.

(11) Noriega, R.; Rivnay, J.; Vandewal, K.; Koch, F. P. V.; Stingelin, N.; Smith, P.; Toney, M. F.; Salleo, A. A General Relationship between Disorder, Aggregation and

Charge Transport in Conjugated Polymers. *Nat. Mater.* **2013**, *12* (11), 1038–1044.

(12) Ran, N. A.; Roland, S.; Love, J. A.; Savikhin, V.; Takacs, C. J.; Fu, Y.-T.; Li, H.; Coropceanu, V.; Liu, X.; Brédas, J.-L.; Bazan, G. C.; Toney, M. F.; Neher, D.; Nguyen, T.-Q. Impact of Interfacial Molecular Orientation on Radiative Recombination and Charge Generation Efficiency. *Nat. Commun.* **2017**, *8* (1), 79.

(13) Rivnay, J.; Steyrleuthner, R.; Jimison, L. H.; Casadei, A.; Chen, Z.; Toney, M. F.; Facchetti, A.; Neher, D.; Salleo, A. Drastic Control of Texture in a High Performance N-Type Polymeric Semiconductor and Implications for Charge Transport. *Macromolecules* **2011**, *44* (13), 5246–5255.

(14) Brown, S. J.; Schlitz, R. A.; Chabinyc, M. L.; Schuller, J. A. Morphology-Dependent Optical Anisotropies in the n -Type Polymer P(NDI2OD-T2). *Phys. Rev. B* **2016**, *94* (16), 165105.

(15) Tremel, K.; Fischer, F. S. U.; Kayunkid, N.; Pietro, R. Di; Tkachov, R.; Kiriy, A.; Neher, D.; Ludwigs, S.; Brinkmann, M. Charge Transport Anisotropy in Highly Oriented Thin Films of the Acceptor Polymer P(NDI2OD-T2). *Adv. Energy Mater.* **2014**, *4* (10), 1301659.

(16) Giussani, E.; Fazzi, D.; Brambilla, L.; Caironi, M.; Castiglioni, C. Molecular Level Investigation of the Film Structure of a High Electron Mobility Copolymer via Vibrational Spectroscopy. *Macromolecules* **2013**, *46* (7), 2658–2670.

(17) Shioya, N.; Shimoaka, T.; Eda, K.; Hasegawa, T. A New Schematic for Poly(3-Alkylthiophene) in an Amorphous Film Studied Using a Novel Structural Index in Infrared Spectroscopy. *Phys. Chem. Chem. Phys.* **2015**, *17* (20), 13472–13479.

(18) Shioya, N.; Shimoaka, T.; Eda, K.; Hasegawa, T. Controlling Mechanism of Molecular Orientation of Poly(3-Alkylthiophene) in a Thin Film Revealed by Using PMAIRS. *Macromolecules* **2017**, *50* (13), 5090–5097.

(19) Liu, X.; Burgers, M. A.; Hsu, B. B. Y.; Coughlin, J. E.; Perez, L. A.; Heeger, A. J.; Bazan, G. C. Molecular Orientation within Thin Films of Isomorphic Molecular Semiconductors. *RSC Adv.* **2015**, *5* (108), 89144–89148.

(20) DeLongchamp, D. M.; Vogel, B. M.; Jung, Y.; Gurau, M. C.; Richter, C. A.; Kirillov, O. A.; Obrzut, J.; Fischer, D. A.; Sambasivan, S.; Richter, L. J.; Lin, E. K. Variations in Semiconducting Polymer Microstructure and Hole Mobility with Spin-Coating Speed. *Chem. Mater.* **2005**, *17* (23), 5610–5612.

(21) Chang, J.-F.; Sun, B.; Breiby, D. W.; Nielsen, M. M.; Sölling, T. I.; Giles, M.; McCulloch, I.; Sirringhaus, H. Enhanced Mobility of Poly(3-Hexylthiophene) Transistors by Spin-Coating from High-Boiling-Point Solvents. *Chem. Mater.* **2004**, *16* (23), 4772–4776.

(22) Aasmundtveit, K. E.; Samuelsen, E. J.; Guldstein, M.; Steinsland, C.; Flornes, O.; Fagermo, C.; Seeberg, T. M.; Pettersson, L. A. A.; Inganäs, O.; Feidenhans'l, R.; Ferrer, S. Structural Anisotropy of Poly(Alkylthiophene) Films. *Macromolecules*

2000, *33* (8), 3120–3127.

(23) Verploegen, E.; Mondal, R.; Bettinger, C. J.; Sok, S.; Toney, M. F.; Bao, Z. Effects of Thermal Annealing upon the Morphology of Polymer-Fullerene Blends. *Adv. Funct. Mater.* **2010**, *20* (20), 3519–3529.

(24) Seifrid, M.; Ford, M. J.; Li, M.; Koh, K. M.; Trefonas, P.; Bazan, G. C. Electrical Performance of a Molecular Organic Semiconductor under Thermal Stress. *Adv. Mater.* **2017**, *29* (12), 1605511.

(25) Rivnay, J.; Mannsfeld, S. C. B.; Miller, C. E.; Salleo, A.; Toney, M. F. Quantitative Determination of Organic Semiconductor Microstructure from the Molecular to Device Scale. *Chemical Reviews*. American Chemical Society October 10, 2012, pp 5488–5519.

(26) Liu, X.; Sun, Y.; Hsu, B. B. Y.; Lorbach, A.; Qi, L.; Heeger, A. J.; Bazan, G. C. Design and Properties of Intermediate-Sized Narrow Band-Gap Conjugated Molecules Relevant to Solution-Processed Organic Solar Cells. *J. Am. Chem. Soc.* **2014**, *136* (15), 5697–5708.

(27) Izawa, T.; Miyazaki, E.; Takimiya, K. Solution-Processible Organic Semiconductors Based on Selenophene-Containing Heteroarenes, 2,7-Dialkyl[1]Benzoselenopheno[3,2-b][1]Benzoselenophenes (C n-BSBSs): Syntheses, Properties, Molecular Arrangements, and Field-Effect Transistor Characteristics. *Chem. Mater.* **2009**, *21* (5), 903–912.

(28) Smilgies, D.-M. Scherrer Grain-Size Analysis Adapted to Grazing-Incidence Scattering with Area Detectors. *J. Appl. Crystallogr.* **2009**, *42* (6), 1030–1034.

III. Characterizing Dynamic Reorganization by an Unusual Method

A. The challenge of solid-state characterization of organic semiconductors

That form follows function is a central principle for the design of organic semiconductors (OSCs). Molecular shape[1,2] directly impacts solid-state organization and the kinetic profiles for achieving organized structures from solution.[3,4] The distances and orientations between subunits within thin films dictate electronic and optical properties[5,6] and thereby the applicability of a given material in emerging optoelectronic applications.[7,8] These considerations are relevant within the context of potential OSC implementation in new classes of lightweight, low-cost and solution-processable technologies such as photovoltaics,[9–13] thermoelectrics,[14,15] thin-film transistors,[16–19] light-emitting devices,[20–22] photodetectors[23] and various types of sensors.[24–27]

In OSC systems with internal modes of reconfiguration, insight into molecular shape is typically attained through single crystal X-ray analysis.[28,29] Information related to the shape and solid-state organization of amorphous systems, which represent an important fraction of materials used in the fabrication organic light-emitting diodes,[30] is currently out of reach. Molecular topology is important as it relates to crystallization of OSCs, especially those which are described by an awkward shape resistant to crystallization.

Understanding both intra- and supramolecular organizations, such as those related to the transformations exhibited by TT, and how they relate to each other would be useful for further refinement of molecular designs as they relate to maximizing solubility and solid-state organization**.** While experiments such as transmission electron microscopy (TEM) or

X-ray scattering provide important information about organization in the bulk, they may be limited by the degree of disorder often present in OSCs**.** TEM can be used to identify various textures within the solid, but resolution at the molecular scale is typically unattainable due to the inherent disorder of solution-processable OSC materials.[31–33] X-ray scattering techniques provide information on molecular order, but are predominantly limited to probing the ordered regions of a solid.[34,35] Aside from certain exceptional cases,[36] *in situ* determination of molecular shape in the solid-state remains elusive.

The molecular OSC TT (Scheme 3-1 and Figure 3-2) is a relevant system to study. TT displays unusual behavior during its transition from solution to the solid-state.[37] Following film formation, the bulk initially forms an amorphous glass, which slowly transitions into a crystalline film, of which there are two polymorphs. This behavior of TT has been attributed to features of its molecular structure, specifically the central tail-to-tail coupled 3,3'-hexylbithiophene donor core. The extra degrees of conformational freedom, compared to traditional covalently rigidified electron-donating units, such as cyclopentadithiophene, give rise to better solubility. It has been proposed that the slow crystallization of TT involves planarization of the internal 3,3'-hexylbithiophene donor core, which involves a ~7 kcal/mol energetic barrier according to theoretical calculations. Characterization of TT thin films via grazing incidence wide-angle X-ray scattering (GIWAXS) confirms that TT is amorphous in the melt and ordered in the solid. GIWAXS diffraction patterns of TT in the melt do not present any peaks, indicating a lack of long-range order. The diffraction pattern of TT in the ordered high-temperature state has a variety of scattering peaks, characteristic of lamellar and π–π stacking. The relatively large number of diffraction peaks also indicates good

intermolecular order. However, due to the superposition of two dimensions in GIWAXS experiments, direct determination of the arrangement of molecules within the unit cell is impossible.

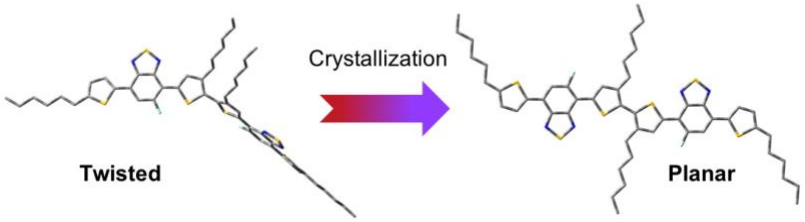

Scheme 3-1. TT has been proposed to twist and adopt a *trans*-planar conformation upon crystallization. Structures are the optimized ground-state equilibrium geometries from density functional theory (DFT) calculations. Hydrogen atoms were removed for clarity.

B. Results and discussion

In this chapter, I will discuss how to address this challenge through the use of solid-state magic-angle spinning (MAS) nuclear magnetic resonance spectroscopy (ssNMR) measurements. These techniques have been used to characterize the shapes of proteins, lipids and other biological structures,[38,39] as well as to understand molecular assembly and disassembly pathways during transitions between solution and solid-state.[40] Their application to OSCs has been relatively limited, such as to distinguish between ordered and disordered regions, and to characterize interfacial structures.[41–45] I examine topological differences at the molecular scale that exist in the melt and ordered states of TT. This characterization is accomplished by tracking changes in ^{13}C chemical shifts and the relative displacements of signals between the amorphous and ordered phases. ^{13}C MAS NMR spectra are analyzed in conjunction with DFT calculations to unravel that crystallization of

TT requires twisting of the dihedral between the central thiophene rings from ~112º to a *trans*-planar conformation.

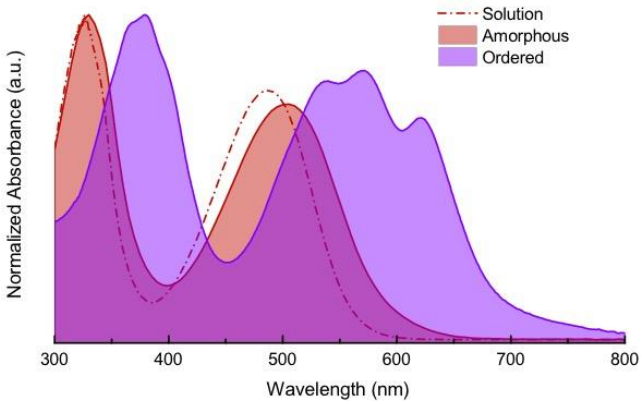

Figure 3-1. In its ordered state, the optical absorbance of TT is noticeably red-shifted relative to those of the amorphous and solution states. The optical absorbances of the solution and amorphous state are very similar, suggesting a similar degree of electronic delocalization along the conjugated backbone.

The absorbance of TT changes between the solution and thin film states, as reproduced in Figure 3-1.[37] Immediately following spin-coating, the absorbance of the film is similar to that of the solution. The absorbance then shows a significant red-shift, which is fully reversible by heating and cooling the film past its melting point.[37] The resemblance of TT absorbance spectra in solution and the melt together with the observed red-shift in ordered lattices have been invoked to suggest planarization of the TT molecule.

Planarization of TT is expected to result in the greatest change in the chemical shifts from the two central-most ^{13}C nuclei (Figure 3-2, purple and yellow dots). Assignments of the signals observed in solution were first performed by analyzing 1D ^{1}H and ^{13}C NMR spectra (Figure 3-S1), 2D $^{1}H\{^{1}H\}$ correlation (Figure 3-S2) and $^{1}H\{^{13}C\}$ heteronuclear multiple-bond correlation (HMBC) NMR spectra (Figures 3-2 and 3-S2).

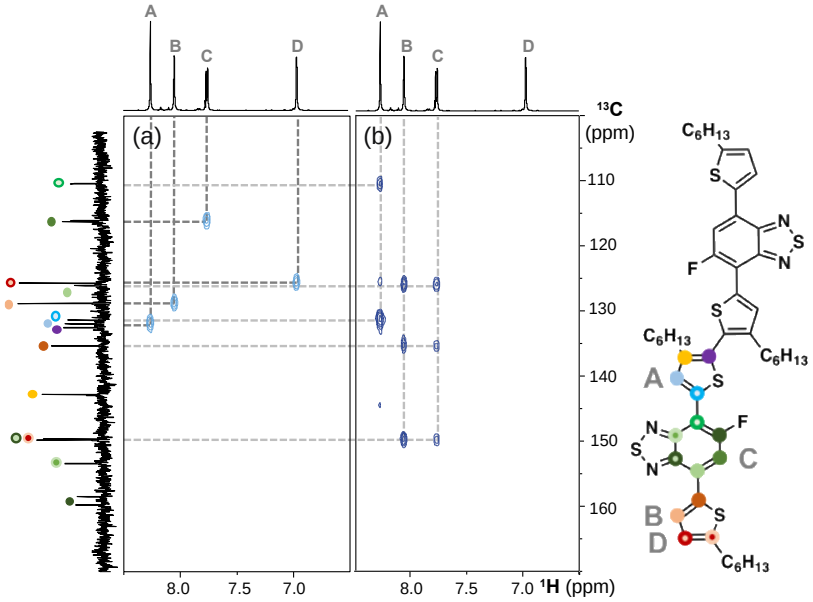

Figure 3-2. Solution-state 2D ^{1}H{^{13}C} HMBC spectra of the aromatic region of TT, acquired using contact times of (a) 3.4 ms and (b) 250 ms, enable isotropic ^{1}H and ^{13}C chemical shifts to be correlated for pairs of *J*-coupled nuclei. The schematic diagram of TT shows ^{13}C moieties assigned according to the colored labels in the left vertical spectrum, and ^{1}H moieties A-D as labelled in the top horizontal spectrum. Dashed grey lines serve as guides to the eye for correlations determined from (a) (dark grey) and (b) (light grey).

The NMR spectroscopic features of TT in the melt are narrow and well resolved (Figure 3-3a). The amorphous state was achieved by heating the sample to 135 ºC (above the melting point, 124 ºC) under a stream of N_2 gas. Signal assignments are straightforward due to the similarity to what is observed in solution (Figure 3-S3). As seen in Figure 3-3a, signals of greatest interest are located at 132.3 ppm (*7*, purple dot) and 141.7 ppm (*5*, yellow dot).

At 118 ºC a single lamellar phase is observed,[37] in which the alkyl sidechains are highly mobile and liquid-like[46,47] on the NMR timescale (ca. 10^{-5} s). This feature is supported by comparison of the ^{13}C CP-MAS NMR spectrum in Figure 3-3b with a static single-pulse ^{13}C

NMR spectrum acquired under otherwise identical conditions (Figure 3-S4); the latter exhibits broad spectral features in the aromatic region (120-165 ppm) that manifest relatively immobile π–π stacked backbones and much narrower signals in the alkyl region (10-30 ppm) from mobile alkyl sidechains. Analogous molecular- and meso-scale characteristics have been observed in lamellar silicate-surfactant phases with stiff covalently cross-linked silicate nanosheets separated by mobile alkyl surfactant chains.[48] Comparison of the 1D ^{13}C spectra (Figure 3-3) of the melt and lamellar phases reveals differences in the isotropic ^{13}C chemical shifts of the TT backbones, depending on whether they are amorphous versus aggregated into π–π stacks. In particular, ^{13}C signals *5* and *7* are displaced in different directions from 141.7 ppm to 139.8 ppm (yellow arrow) and from 132.3 ppm to 139.8 ppm (purple arrow), respectively. Though these two signals overlap at 118 ºC, a quantitative 1D ^{13}C MAS spectrum of TT (Figure 3-S5) and separate DFT calculations (discussed below) corroborate their assignments. This is further supported by 2D $^{13}C\{^{1}H\}$ heteronuclear correlation (HETCOR) spectra acquired with different CP contact times (Figure 3-S6), in which the intramolecular ^{13}C-^{1}H proximities of carbon atoms *5* and *7* are distinguished from their peripheral counterparts (*6* and *12*).

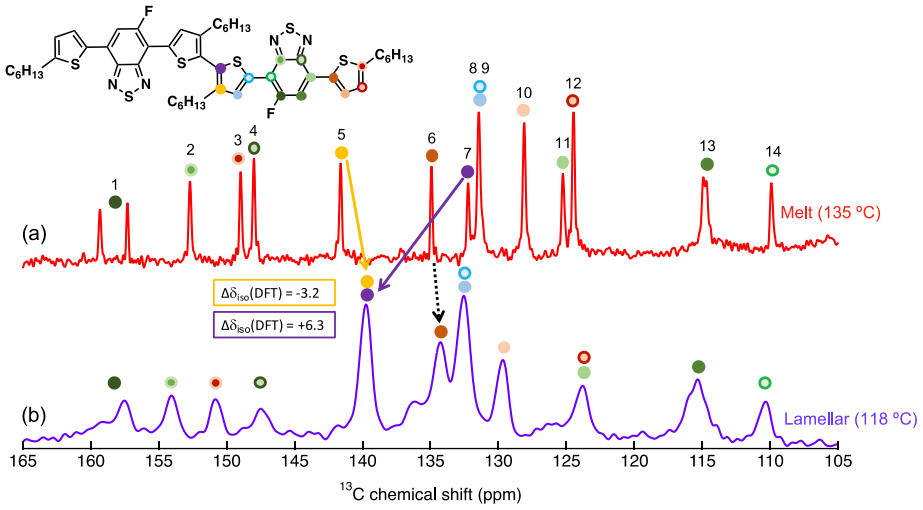

Figure 3-3. Aromatic regions of (a) the static single-pulse ^{13}C NMR spectrum of the melt state at 135 ºC and (b) the $^{13}C\{^{1}H\}$ CP-MAS NMR spectrum of the lamellar phase at 118 ºC. Displacements of the respective ^{13}C isotropic chemical shifts between (a) and (b) suggest different topologies of TT in the two states associated with different conformations or extents of π–π stacking of the conjugated backbones. The color-coded ^{13}C signal assignments are the same as shown in Figure 3-2.

The NMR analysis to this point yields little direct information regarding molecular topology. However, in combination with DFT modeling, the experimental isotropic ^{13}C chemical shifts associated with the melt and lamellar TT structures can be compared with DFT-calculated ^{13}C shieldings for twisted and planar TT backbone conformations (Scheme 3-1). The gauge-independent atomic orbital method of DFT was used with the semi-empirically tuned ωB97XD functional and 6-311+G(2d,p) basis set.[49] The dielectric environment of an OSC is modeled with the conductor-like polarizable continuum model with the static dielectric constant as $\varepsilon = 3.5$ and the dynamic dielectric constant as $\varepsilon_{inf} = 2$.[50,51] Regression analyses were carried out by comparing experimental ^{13}C chemical shifts against the DFT-calculated ^{13}C shieldings for the twisted and planar conformers of TT

(Figure 3-S7).[52–55] Comparison of the experimental ^{13}C chemical shifts in the melt and ^{13}C shieldings of the twisted conformer of TT resulted in a regression coefficient of $R^2 = 0.98$. A similar analysis and comparison for the lamellar phase and ^{13}C shieldings of the planar conformer of TT resulted in $R^2 = 0.99$. Within the resolution limits of the NMR data and the validities of model assumptions, the level of agreement is noteworthy. Further accuracy in the calculation of chemical shieldings requires taking into account intermolecular contacts[56] that are not possible to model for an isolated molecule. This approach is also restricted to materials whose NMR spectra do not contain an excessive number of overlapping signals, which may be difficult to clearly resolve.

Differences in the experimental isotropic ^{13}C chemical shifts of the TT backbone between the melt and lamellar phases ($\Delta\delta_{iso}$ Expt., Figure 3-4) are also correlated to differences in molecular conformation and shape. While most $\Delta\delta_{iso}$ values are within ±2 ppm (Figure 3-4, grey region), the ^{13}C atoms of most interest (signals *5* and *7*, highlighted in green) are predicted to be displaced by -3.2 ppm and +6.3 ppm, respectively, compared to experimental values of -1.9 ppm and +7.5 ppm. These results are consistent with changes of the TT backbone geometry involving a transition from twisted to *trans*-planar conformations. The ssNMR results and DFT calculations are also consistent with the observed differences in the optical properties of TT (Figure 3-1). As TT adopts a planar molecular topology, the degree of electronic delocalization increases.

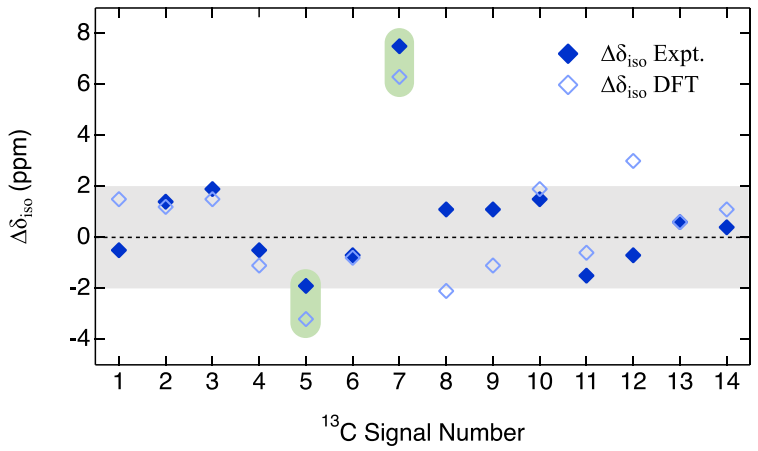

Figure 3-4. Relative differences in isotropic ^{13}C chemical shifts ($\Delta\delta_{iso}$) of the TT backbone nuclei between the melt and lamellar phases, as determined by high temperature ^{13}C NMR and from DFT. Most signals differ by < 2 ppm (grey band), while those from carbon atoms *5* and *7* (green bands) show more pronounced differences. The discrepancies associated with signals *8*, *9* and *12* likely arise from differences in the orientations of the alkyl chains relative to the structures used for DFT calculations.

C. Conclusion

The combination of *in situ* NMR with DFT-based modeling provides new molecular-level insights that manifest important topological changes that were previously only hypothesized based on differences in macroscopic optical properties. Specifically, the combined NMR+DFT approach identifies a twisted molecular topology of TT in the melt state, while the molecule is found to adopt a planar topology in the lamellar phase. Refinement of these methods as they relate to solid-state structures of OSCs is likely to reveal further information regarding the impact of intramolecular features and long-range organization on processes, such as charge carrier generation or transport, which ultimately determine technological feasibility. For example, the techniques described in this chapter may be extended to probe the effects of polymer architecture on charge carrier mobility. In

the case of TT, the energy cost for planarization is compensated by lattice interactions that decrease the free energy relative to the amorphous state. From a practical perspective, such considerations are expected to enable control of solid-state structural features at the level of molecular design, enabling device performance to be decoupled from processing conditions. Potential advantages of such materials include development of device active layers that can be processed through deposition methods that are not solvent-dependent. Processing methods that are solvent-independent are also likely to avoid pitfalls of kinetic trapping during film formation such as those discussed in the previous chapter. Furthermore, solid-state organization that is driven by intermolecular interactions is also likely to results in materials that are more thermally stable, for example in contexts such as those described in the first chapter.

D. Experimental and Supplementary Information

UV-visible absorption spectroscopy: UV-vis absorption spectra were recorded on a Perkin Elmer Lambda 750 UV-Vis spectrometer. The solution spectrum was determined by dissolving TT in chloroform at 0.01 mg/mL. Thin film absorbance measurements were performed using glass as the substrate, and the material was spin coated for 60 s at 1500 rpm at 10 mg/mL in chloroform. Absorbance measurements of the ordered solid and amorphous state were performed at ~ 115 ºC and after quickly cooling to room temperature from ~ 135 ºC. Thin film heating was accomplished by using a heated sample mount. The temperature was measured with an external thermocouple probe.

Solution-state NMR spectroscopy*:* Solution-state ^{1}H and ^{13}C NMR were used to characterize TT. Approximately 10 mg of TT dissolved in 1,1,2,2-tetrachloroethane-d_2 and transferred into a 4 mm NMR tube. All NMR experiments were carried out at room temperature on a Bruker 18.8 T AVANCE-II NMR spectrometer (^{1}H and ^{13}C Larmor frequencies were 800.24 MHz and 200 MHz, respectively) equipped with 4 mm B-B-O probe. The ^{1}H and ^{13}C 90° pulse lengths were of 11 μs and 9 μs, respectively. One-dimensional (1D) ^{1}H NMR spectrum was acquired by co-adding 8 transients using a relaxation delay of 2 s. 1D ^{13}C NMR spectrum was acquired by co-adding1024 transients using a relaxation delay of 2 s corresponding to an experimental time of 1h. WALTZ-16 heteronuclear decoupling[1] was used during the acquisition of ^{13}C spectrum with ^{1}H 180° pulse duration of 60 μs. To identify and distinguish *J*-mediated through-bond ^{1}H-^{1}H and ^{1}H-^{13}C moieties, two-dimensional (2D) $^{1}H\{^{1}H\}$ correlation (COSY) and 2D $^{1}H\{^{13}C\}$ heteronuclear multiple-bond correlation (HMBC) NMR spectra were acquired and analyzed.

2D $^{1}H\{^{1}H\}$ spectrum was acquired using 128 t_1 increments using an incremental time of 114 μs, each by co-adding 2 transients, with a recycle delay of 2 s corresponding to an experimental time of 16 mins. 2D $^{1}H\{^{13}C\}$ HMBC spectra were acquired using 3.4 ms ($1/2J_{CH}$, where, J_{CH} = 145 Hz) and 250 ms (i.e., $1/2J_{CH}$, where, J_{CH} = 2 Hz) mixing times, each using 76 t_1 increments with an incremental time of 14.6 μs and by the co-addition of 96 transients with a recycle delay of 2 s corresponding to a total experimental time of 7 h. All ^{1}H and ^{13}C experimental shifts are calibrated with respect to ^{1}H and ^{13}C signals of 1,1,2,2-tetrachloroethane-d_2 at 6.0 and 73.8 ppm, respectively.

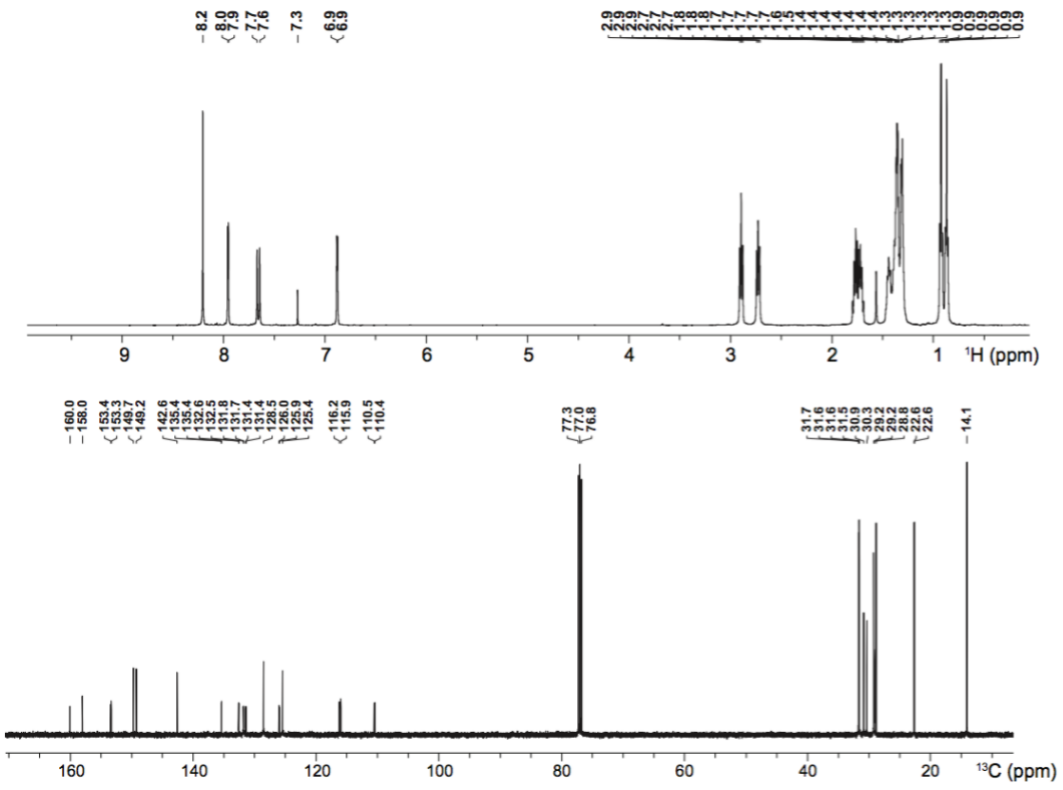

Figure 3-S1. Solution-state ^{1}H and ^{13}C NMR spectra of TT dissolved in 1,1,2,2-tetrachloroethane-d_2 acquired at 18.8 T (^{1}H 800 MHz) at room temperature.

Solution-state ^{1}H and ^{13}C chemical shifts and splittings for the backbone moieties of TT are listed below.

^{1}H solution-state NMR in 1,1,2,2-tetrachloroethane-d_2 (ppm): 8.26 (s, 2H), 8.05 (d, J=3.2 Hz, 2H), 7.77 (d, J=12.9 Hz, 2H), 6.97 (d, J=2.9 Hz, 2H)

^{13}C solution-state NMR in 1,1,2,2-tetrachloroethane-d_2, δ (ppm): 159.2, 153.5, 149.9, 149.7, 142.9, 135.4, 132.7, 132.0, 131.5, 129.0, 126.2, 125.8, 116.3, 110.5

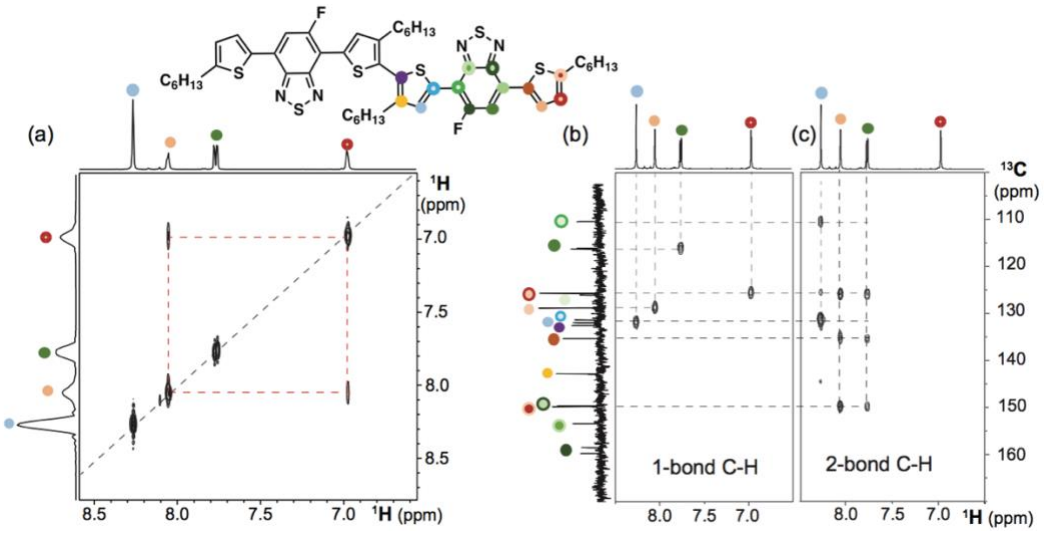

Figure 3-S2. Solution-state 2D ^{1}H{^{1}H} correlation (COSY) spectrum of TT dissolved in 1,1,2,2-tetrachloroethane-d_2 acquired at 18.8 T (^{1}H 800 MHz) at room temperature. Off diagonal correlation intensities shown in dashed red lines depict the through-bond interactions between thiophene protons.

Solid-state MAS NMR spectroscopy: A powder of TT was packed into a 4 mm (outer diameter) zirconia rotor fitted with Teflon insert and a ceramic cap fitted with a rubber *o*-ring to ensure close fitting of the sample. All variable temperature 1D and 2D MAS NMR spectra of TT were acquired on a 11.7 T Bruker AVANCE-II NMR spectrometer equipped with 4 mm H-X-Y probehead and Bruker VT control unit to regulate probe temperature. The ^{1}H and ^{13}C 90º pulse durations were 2.5 μs and 4.0 μs, respectively. To ensure the melt state of TT, single-pulse ^{13}C NMR spectrum was acquired at 135 ºC under a static condition by co-adding 2048 transients using a relaxation delay of 2 s corresponding to an experimental

time of 2 h. For TT in the solid state, 1D $^{13}C\{^{1}H\}$ CP-MAS spectra were acquired at 118 ºC using 0.1 ms and 2 ms of CP contact times under 8 kHz MAS conditions using a stream of N_2 gas. Cross polarization involves the simultaneous excitation of ^{1}H and ^{13}C nuclei to enhance the signals of the latter. Heteronuclear decoupling was applied during acquisition of ^{13}C spectra using SPINAL64 sequence[58] using 2048 co-added transients with a 3 s recycle delay, corresponding to an experimental time of 2 h each. To characterize spatially proximate dipole-dipole coupled ^{1}H-^{13}C pairs, 2D $^{13}C\{^{1}H\}$ heteronuclear correlation (HETCOR) NMR spectra were acquired using a short (0.1 ms) and long (2 ms) CP contact times. 2D $^{13}C\{^{1}H\}$ HETCOR NMR spectra were acquired using 32 t_1 increments using an incremental time of 80 μs, each by co-adding 256 transients with a relaxation delay of 3 s corresponding to an experimental time of 7 h each.

All ^{1}H and ^{13}C experimental shifts are calibrated with respect to neat TMS using adamantane as an external reference (higher ppm ^{13}C resonance, 35.8 ppm[59] and the ^{1}H resonance, 1.85 ppm[60]).

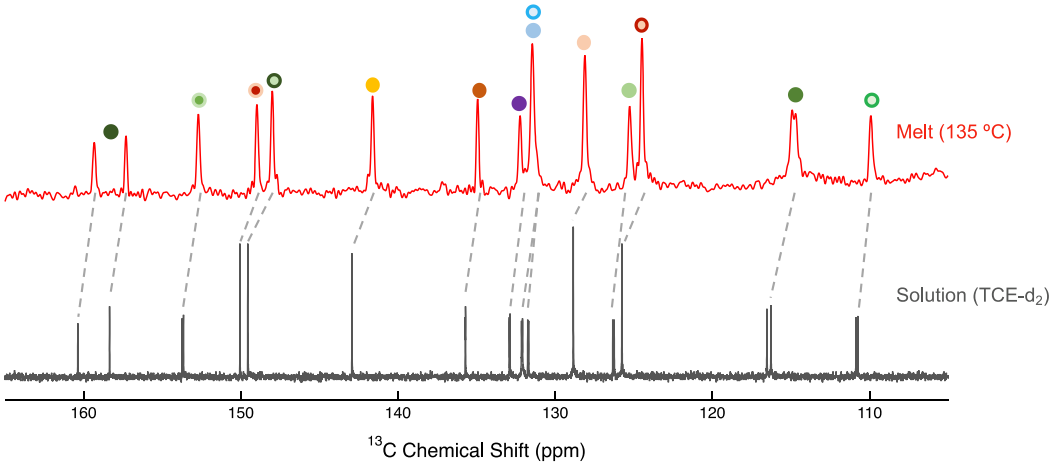

Figure 3-S3. Comparison of single-pulse ^{13}C NMR spectrum of TT acquired at 135 ºC (melt) and the analogous ^{13}C NMR spectrum of TT dissolved in 1,1,2,2-tetrachloroethane-d_2 acquired at room temperature.

Aromatic ^{13}C chemical shifts of TT measured at 135 ºC (melt) and at 118 ºC (ordered solid) are given below.

^{13}C NMR in the melt (135 ºC), δ (ppm): 159.4, 157.4, 152.8, 149.1, 148.1, 141.7, 135.0, 132.3, 131.5, 131.5, 128.2, 125.3, 124.6, 114.9, 110.0

^{13}C solid-state NMR of the solid (118 ºC), δ (ppm): 159.2, 157.6, 154.2, 150.9, 147.6, 139.8, 139.8, 134.3, 132.6, 132.6, 129.7, 123.8, 123.8, 115.4, 110.4

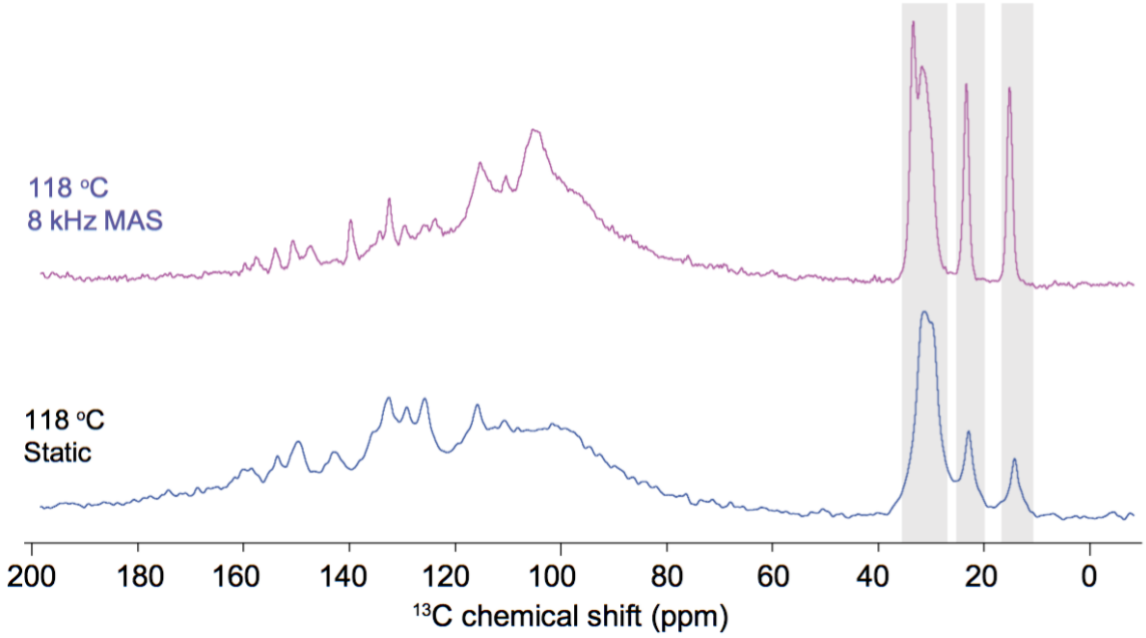

Figure 3-S4. Solid-state single-pulse ^{13}C NMR spectra of TT acquired at 11.7 T and 118 ºC using MAS (top) and static (bottom) conditions. Shaded regions highlight similarities in signal intensities and line widths and suggest the presence of disordered alkyl side chains, whereas the broad spectral features observed in the aromatic region (110 – 160 ppm) of the spectrum acquired under static conditions suggest well ordered, π-π stacked TT backbones.

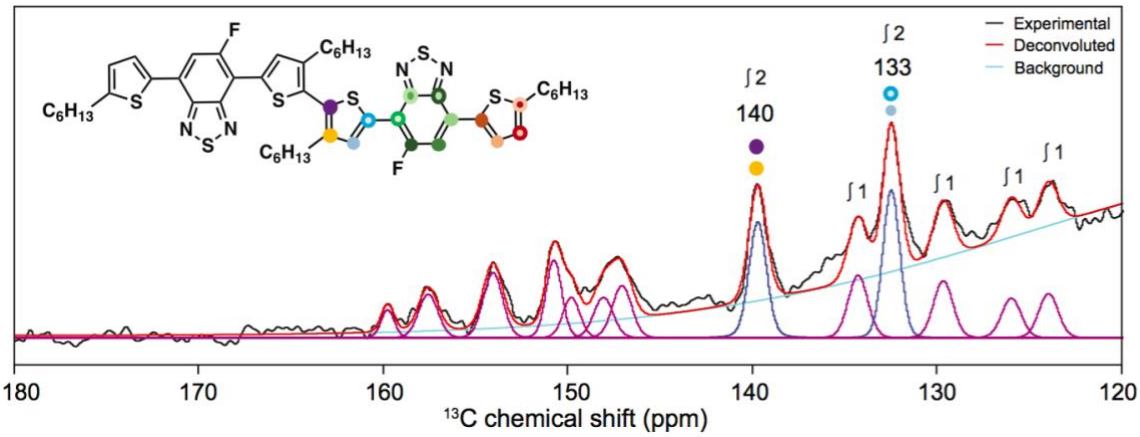

Figure 3-S5. Solid-state single-pulse ^{13}C NMR spectrum of TT acquired at 11.7 T and 118 ºC using high-power ^{1}H-decoupling. Integrals measured from the deconvolution of the spectrum reveal that the signals at 140 and 133 ppm are the overlapping contributions from two different carbon signals.

For TT in the lamellar state at 118 ºC, the local structures of the central and peripheral thiophene groups are elucidated by analyzing 2D $^{13}C\{^{1}H\}$ HETCOR NMR spectra (Figure 3-S6); in the spectrum acquired using 0.1 ms CP contact time, correlated signal intensities at 134 ppm (^{13}C) and 7.6 ppm (^{1}H) correspond to directly bonded ^{13}C-^{1}H of central thiophene (blue dot), and at 130 ppm (^{13}C) and 7.4 ppm (^{1}H) and 115 ppm (^{13}C) and 6.9 ppm (^{1}H) indicate the directly bonded ^{13}C-^{1}H in fluorobenzothiadiazole and thiophene end groups, respectively. In the 2D $^{13}C\{^{1}H\}$ HETCOR NMR spectrum acquired using 2 ms of CP contact time, correlation intensities originate from thiophene ^{13}C and alkyl sidechain ^{1}H moieties are observed as depicted by dashed horizontal and vertical lines in Figure 3-S6b.

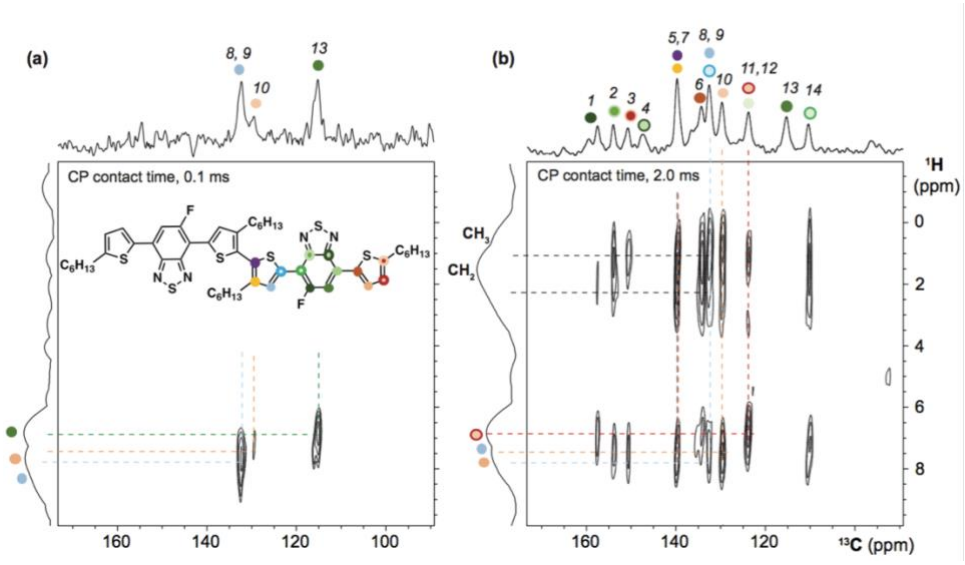

Figure 3-S6. Solid-state 2D $^{13}C\{^{1}H\}$ HETCOR NMR spectrum recorded at 11.7 T and at 118 ºC using (a) 0.1 ms and (b) 2 ms of CP contact times, respectively.

DFT calculations: All calculations were performed using the Gaussian 09 software package.[61] The B3LYP functional and 6-31G(d,p) basis set were used to optimize the ground-state equilibrium geometry of TT. For the planar conformation, the central S-C-C-S dihedral was frozen at 180º and the rest of the structure was allowed to optimize the ground-state equilibrium geometry. The twisted conformation of TT was allowed to relax to the lowest energy conformation without any constraints. For each conformer of TT, the range-separation parameter ω in the ωB97XD functional was tuned using the gap tuning procedure.[62] The structures were subsequently optimized to their ground-state equilibrium geometries using the tuned ωB97XD/6-31G(d,p) functional and basis set by the same methods described above; $\omega = 0.1253$ bohr^{-1} for the twisted conformer and $\omega = 0.1081$ bohr^{-1} for the trans-planar conformer. These optimized geometries were used to calculate magnetic shieldings using the gauge-independent atomic orbital (GIAO) method in a

conductor-like polarizable continuum model (CPCM)[63] for a conjugated organic material (where the static dielectric constant is set to $\varepsilon = 3.5$ and the dynamic dielectric constant is set to $\varepsilon_{inf} = 2$)[64] with the tuned ωB97XD functional and 6-311+G(2d,p) basis set. Plots of experimental ^{13}C chemical shifts versus GIAO DFT-calculated NMR chemical shifts are shown in Figure 3-S7 for the planar and twisted TT conformations.

Based on calculations of different possible rota-mers for both the twisted and planar confor-mations of TT, planarization of the molecule may also involve a flip of the fluorobenzothiadiazole (FBT) heterocycles and outer thiophene rings. This additional reconfiguration is reasonable, as single crystal data for similar compounds have shown a multitude of rotamer populations.[65-67]

Computationally predicted chemical shieldings, σ_{iso}, can be compared to experimental isotropic chemical shifts, δ_{iso}, by using the following conversion,[68-73]

$$\delta_{iso} = \frac{intercept - \sigma_{iso}}{-slope} \qquad (1)$$

where *intercept* and *slope* are the intercept and slope determined from linear regression analysis in Figure 3-S7.

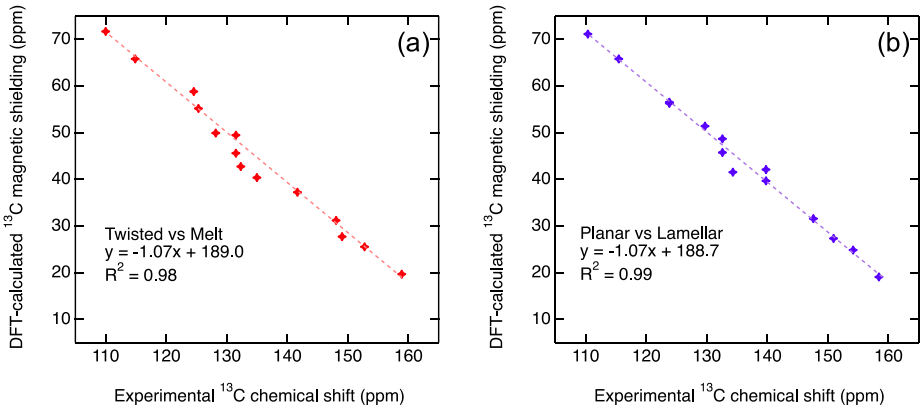

Figure 3-S7. Plots of DFT-calculated ^{13}C chemical shieldings versus experimental ^{13}C chemical shifts obtained for the twisted (a) and planar (b) conformations of TT models from the high-temperature ^{13}C NMR spectra acquired at 135 ºC and 118 ºC, respectively. Regression analyses are presented in figure insets, which depict reasonably good agreements with R^2 values 0.98 and 0.99 for the twisted and planar conformers of TT, respectively.

DFT-calculated isotropic ^{13}C chemical shieldings for the backbone carbon atoms of TT are given below.

Twisted conformer, σ_{iso} (ppm): 19.6941, 25.5663, 27.7351, 31.2094, 37.257, 40.3939, 42.7596, 45.6088, 49.4673, 49.9177, 55.1814, 58.8164, 65.7932, 71.682

Planar conformer, σ_{iso} (ppm): 19.1113, 24.8516, 27.3565, 31.6064, 39.6791, 41.5304, 42.1121, 45.7494, 48.6781, 51.4214, 56.2908, 56.5454, 65.8058, 71.1200

E. References

(1) Conboy, G.; Spencer, H. J.; Angioni, E.; Kanibolotsky, A. L.; Findlay, N. J.; Coles, S. J.; Wilson, C.; Pitak, M. B.; Risko, C.; Coropceanu, V.; Brédas, J.-L.; Skabara, P. J. To Bend or Not to Bend – Are Heteroatom Interactions within Conjugated Molecules Effective in Dictating Conformation and Planarity? *Mater. Horiz.* **2016**, *3* (4), 333–339.

(2) Liu, X.; Sun, Y.; Hsu, B. B. Y.; Lorbach, A.; Qi, L.; Heeger, A. J.; Bazan, G. C. Design and Properties of Intermediate-Sized Narrow Band-Gap Conjugated Molecules Relevant to Solution-Processed Organic Solar Cells. *J. Am. Chem. Soc.* **2014**, *136* (15), 5697–5708.

(3) Liu, X.; Burgers, M. A.; Hsu, B. B. Y.; Coughlin, J. E.; Perez, L. A.; Heeger, A. J.; Bazan, G. C. Molecular Orientation within Thin Films of Isomorphic Molecular Semiconductors. *RSC Adv* **2015**, *5* (108), 89144–89148.

(4) Seifrid, M. T.; Oosterhout, S. D.; Toney, M. F.; Bazan, G. C. Kinetic Versus Thermodynamic Orientational Preferences for a Series of Isomorphic Molecular Semiconductors. *ACS Omega* **2018**, *3* (8), 10198–10204.

(5) Djurovich, P. I.; Mayo, E. I.; Forrest, S. R.; Thompson, M. E. Measurement of the Lowest Unoccupied Molecular Orbital Energies of Molecular Organic Semiconductors. *Org. Electron.* **2009**, *10* (3), 515–520.

(6) Roncali, J. Synthetic Principles for Bandgap Control in Linear π-Conjugated Systems. *Chem. Rev.* **1997**, *97* (1), 173–206.

(7) Mas-Torrent, M.; Rovira, C. Role of Molecular Order and Solid-State Structure in Organic Field-Effect Transistors. *Chem. Rev.* **2011**, *111* (8), 4833–4856.

(8) Bredas, J. L.; Calbert, J. P.; da Silva Filho, D. A.; Cornil, J. Organic Semiconductors: A Theoretical Characterization of the Basic Parameters Governing Charge Transport. *Proc. Natl. Acad. Sci.* **2002**, *99* (9), 5804–5809.

(9) Roncali, J.; Leriche, P.; Blanchard, P. Molecular Materials for Organic Photovoltaics: Small Is Beautiful. *Adv. Mater.* **2014**, *26* (23), 3821–3838.

(10) Li, G.; Zhu, R.; Yang, Y. Polymer Solar Cells. *Nature Photonics*. Nature Publishing Group March 1, 2012, pp 153–161.

(11) Zhou, H.; Yang, L.; You, W. Rational Design of High Performance Conjugated Polymers for Organic Solar Cells. *Macromolecules*. American Chemical Society January 24, 2012, pp 607–632.

(12) Mazzio, K. A.; Luscombe, C. K. The Future of Organic Photovoltaics. *Chem. Soc. Rev.* **2015**, *44* (1), 78–90.

(13) He, Z.; Wu, H.; Cao, Y. Recent Advances in Polymer Solar Cells: Realization of High Device Performance by Incorporating Water/Alcohol-Soluble Conjugated Polymers as Electrode Buffer Layer. *Adv. Mater.* **2014**, *26* (7), 1006–1024.

(14) Russ, B.; Glaudell, A.; Urban, J. J.; Chabinyc, M. L.; Segalman, R. A. Organic Thermoelectric Materials for Energy Harvesting and Temperature Control. *Nature Reviews Materials*. Nature Publishing Group October 2, 2016, p 16050.

(15) Chen, Y.; Zhao, Y.; Liang, Z. Solution Processed Organic Thermoelectrics: Towards Flexible Thermoelectric Modules. *Energy and Environmental Science*. The Royal Society of Chemistry February 4, 2015, pp 401–422.

(16) Sirringhaus, H. 25th Anniversary Article: Organic Field-Effect Transistors: The Path beyond Amorphous Silicon. *Adv. Mater. Deerfield Beach Fla* **2014**, *26* (9), 1319–1335.

(17) Zhang, W.; Liu, Y.; Yu, G. Heteroatom Substituted Organic/Polymeric Semiconductors and Their Applications in Field-Effect Transistors. *Adv. Mater.* **2014**, *26* (40), 6898–6904.

(18) Bisri, S. Z.; Piliego, C.; Gao, J.; Loi, M. A. Outlook and Emerging Semiconducting Materials for Ambipolar Transistors. *Adv. Mater.* **2014**, *26* (8), 1176–1199.

(19) Biniek, L.; Schroeder, B. C.; Nielsen, C. B.; McCulloch, I. Recent Advances in High Mobility Donor–Acceptor Semiconducting Polymers. *J. Mater. Chem.* **2012**, *22* (30), 14803.

(20) Geffroy, B.; le Roy, P.; Prat, C. Organic Light-Emitting Diode (OLED) Technology: Materials, Devices and Display Technologies. *Polym. Int.* **2006**, *55* (6), 572–582.

(21) Bernius, M. T.; Inbasekaran, M.; O'Brien, J.; Wu, W. Progress with Light-Emitting Polymers. *Adv. Mater.* **2000**, *12* (23), 1737–1750.

(22) Reineke, S.; Lindner, F.; Schwartz, G.; Seidler, N.; Walzer, K.; Lüssem, B.; Leo, K. White Organic Light-Emitting Diodes with Fluorescent Tube Efficiency. *Nature* **2009**, *459* (7244), 234–238.

(23) Baeg, K. J.; Binda, M.; Natali, D.; Caironi, M.; Noh, Y. Y. Organic Light Detectors: Photodiodes and Phototransistors. *Advanced Materials*. Wiley-Blackwell August 21, 2013, pp 4267–4295.

(24) Rivnay, J.; Owens, R. M.; Malliaras, G. G. The Rise of Organic Bioelectronics. *Chem. Mater.* **2014**, *26* (1), 679–685.

(25) Someya, T.; Bao, Z.; Malliaras, G. G. The Rise of Plastic Bioelectronics. *Nature*. Nature Publishing Group December 15, 2016, pp 379–385.

(26) Inal, S.; Rivnay, J.; Suiu, A. O.; Malliaras, G. G.; McCulloch, I. Conjugated Polymers in Bioelectronics. *Acc. Chem. Res.* **2018**, *51* (6), 1368–1376.

(27) Hua, Q.; Sun, J.; Liu, H.; Bao, R.; Yu, R.; Zhai, J.; Pan, C.; Wang, Z. L. Skin-Inspired Highly Stretchable and Conformable Matrix Networks for Multifunctional Sensing. *Nat. Commun.* **2018**, *9* (1), 244.

(28) Van Der Poll, T. S.; Zhugayevych, A.; Chertkov, E.; Bakus, R. C.; Coughlin, J. E.; Teat, S. J.; Bazan, G. C.; Tretiak, S. Polymorphism of Crystalline Molecular Donors for Solution-Processed Organic Photovoltaics. *J. Phys. Chem. Lett.* **2014**, *5* (15), 2700–2704.

(29) Coughlin, J. E.; Zhugayevych, A.; Bakus, R. C.; van der Poll, T. S.; Welch, G. C.; Teat, S. J.; Bazan, G. C.; Tretiak, S. A Combined Experimental and Theoretical Study of Conformational Preferences of Molecular Semiconductors. *J. Phys. Chem. C* **2014**, *118* (29), 140627161810001.

(30) Tao, Y.; Yang, C.; Qin, J. Organic Host Materials for Phosphorescent Organic Light-Emitting Diodes. *Chemical Society Reviews*. The Royal Society of Chemistry April 18, 2011, pp 2943–2970.

(31) Yang, X.; Loos, J.; Veenstra, S. C.; Verhees, W. J. H.; Wienk, M. M.; Kroon, J. M.; Michels, M. A. J.; Janssen, R. A. J. Nanoscale Morphology of High-Performance Polymer Solar Cells. *Nano Lett.* **2005**, *5* (4), 579–583.

(32) Brinkmann, M.; Rannou, P. Molecular Weight Dependence of Chain Packing and Semicrystalline Structure in Oriented Films of Regioregular Poly(3-

Hexylthiophene)Revealed by High-Resolution Transmission Electron Microscopy. *Macromolecules* **2009**, *42* (4), 1125–1130.

(33) Takacs, C. J.; Treat, N. D.; Krämer, S.; Chen, Z.; Facchetti, A.; Chabinyc, M. L.; Heeger, A. J. Remarkable Order of a High-Performance Polymer. *Nano Lett.* **2013**, *13* (6), 2522–2527.

(34) Rivnay, J.; Mannsfeld, S. C. B.; Miller, C. E.; Salleo, A.; Toney, M. F. Quantitative Determination of Organic Semiconductor Microstructure from the Molecular to Device Scale. *Chemical Reviews*. American Chemical Society October 10, 2012, pp 5488–5519.

(35) McNeill, C. R.; Ade, H. Soft X-Ray Characterisation of Organic Semiconductor Films. *J Mater Chem C* **2013**, *1* (2), 187–201.

(36) Takacs, C. J.; Brady, M. A.; Treat, N. D.; Kramer, E. J.; Chabinyc, M. L. Quadrites and Crossed-Chain Crystal Structures in Polymer Semiconductors. *Nano Lett.* **2014**, *14* (6), 3096–3101.

(37) Zhou, C.; Cui, Q.; McDowell, C.; Seifrid, M.; Chen, X.; Brédas, J. L.; Wang, M.; Huang, F.; Bazan, G. C. Topological Transformation of π-Conjugated Molecules Reduces Resistance to Crystallization. *Angew. Chem. - Int. Ed.* **2017**, *56* (32), 9318–9321.

(38) McDermott, A. Structure and Dynamics of Membrane Proteins by Magic Angle Spinning Solid-State NMR. *Annu. Rev. Biophys.* **2009**, *38* (1), 385–403.

(39) Tycko, R. Solid-State NMR Studies of Amyloid Fibril Structure. *Annu. Rev. Phys. Chem.* **2011**, *62* (1), 279–299.

(40) Reddy, G. N. M.; Huqi, A.; Iuga, D.; Sakurai, S.; Marsh, A.; Davis, J. T.; Masiero, S.; Brown, S. P. Coexistence of Distinct Supramolecular Assemblies in Solution and in the Solid State. *Chem. - Eur. J.* **2017**, *23* (10), 2235.

(41) Cochran, J. E.; Junk, M. J. N.; Glaudell, A. M.; Miller, P. L.; Cowart, J. S.; Toney, M. F.; Hawker, C. J.; Chmelka, B. F.; Chabinyc, M. L. Molecular Interactions and Ordering in Electrically Doped Polymers: Blends of PBTTT and F 4 TCNQ. *Macromolecules* **2014**, *47* (19), 6836–6846.

(42) Do, K.; Saleem, Q.; Ravva, M. K.; Cruciani, F.; Kan, Z.; Wolf, J.; Hansen, M. R.; Beaujuge, P. M.; Brédas, J. L. Impact of Fluorine Substituents on π-Conjugated Polymer Main-Chain Conformations, Packing, and Electronic Couplings. *Adv. Mater.* **2016**, *28* (37), 8197–8205.

(43) Melnyk, A.; Junk, M. J. N.; McGehee, M. D.; Chmelka, B. F.; Hansen, M. R.; Andrienko, D. Macroscopic Structural Compositions of π-Conjugated Polymers: Combined Insights from Solid-State NMR and Molecular Dynamics Simulations. *J. Phys. Chem. Lett.* **2017**, *8* (17), 4155–4160.

(44) Nieuwendaal, R. C.; Ro, H. W.; Germack, D. S.; Kline, R. J.; Toney, M. F.; Chan, C. K.; Agrawal, A.; Gundlach, D.; VanderHart, D. L.; Delongchamp, D. M. Measuring Domain Sizes and Compositional Heterogeneities in P3HT-PCBM Bulk Heterojunction Thin Films with 1H Spin Diffusion NMR Spectroscopy. *Adv. Funct. Mater.* **2012**, *22* (6), 1255–1266.

(45) Nieuwendaal, R. C.; DeLongchamp, D. M.; Richter, L. J.; Snyder, C. R.; Jones, R. L.; Engmann, S.; Herzing, A.; Heeney, M.; Fei, Z.; Sieval, A. B.; Hummelen, J. C.

Characterization of Interfacial Structure in Polymer-Fullerene Bulk Heterojunctions via 13C{2H} Rotational Echo Double Resonance NMR. *Phys. Rev. Lett.* **2018**, *121* (2), 026101.

(46) Malik, S.; Nandi, A. K. Crystallization Mechanism of Regioregular Poly(3-Alkyl Thiophene)S. *J. Polym. Sci. Part B Polym. Phys.* **2002**, *40* (18), 2073–2085.

(47) Causin, V.; Marega, C.; Marigo, A.; Valentini, L.; Kenny, J. M. Crystallization and Melting Behavior of Poly(3-Butylthiophene), Poly(3-Octylthiophene), and Poly(3-Dodecylthiophene). *Macromolecules* **2005**, *38* (2), 409–415.

(48) Brouwer, D. H.; Cadars, S.; Eckert, J.; Liu, Z.; Terasaki, O.; Chmelka, B. F. A General Protocol for Determining the Structures of Molecularly Ordered but Noncrystalline Silicate Frameworks. *J. Am. Chem. Soc.* **2013**, *135* (15), 5641–5655.

(49) Sun, H.; Zhong, C.; Brédas, J.-L. Reliable Prediction with Tuned Range-Separated Functionals of the Singlet–Triplet Gap in Organic Emitters for Thermally Activated Delayed Fluorescence. *J. Chem. Theory Comput.* **2015**, *11* (8), 3851–3858.

(50) Sun, H.; Ryno, S.; Zhong, C.; Ravva, M. K.; Sun, Z.; Körzdörfer, T.; Brédas, J.-L. Ionization Energies, Electron Affinities, and Polarization Energies of Organic Molecular Crystals: Quantitative Estimations from a Polarizable Continuum Model (PCM)-Tuned Range-Separated Density Functional Approach. *J. Chem. Theory Comput.* **2016**, *12* (6), 2906–2916.

(51) Takano, Y.; Houk, K. N. Benchmarking the Conductor-like Polarizable Continuum Model (CPCM) for Aqueous Solvation Free Energies of Neutral and Ionic Organic Molecules. *J. Chem. Theory Comput.* **2005**, *1* (1), 70–77.

(52) Lodewyk, M. W.; Siebert, M. R.; Tantillo, D. J. Computational Prediction Of1H And13C Chemical Shifts: A Useful Tool for Natural Product, Mechanistic, and Synthetic Organic Chemistry. *Chemical Reviews*. American Chemical Society March 14, 2012, pp 1839–1862.

(53) Pierens, G. K. 1H and 13C NMR Scaling Factors for the Calculation of Chemical Shifts in Commonly Used Solvents Using Density Functional Theory. *J. Comput. Chem.* **2014**, *35* (18), 1388–1394.

(54) Benassi, E. Benchmarking of Density Functionals for a Soft but Accurate Prediction and Assignment Of1H And13C NMR Chemical Shifts in Organic and Biological Molecules. *J. Comput. Chem.* **2017**, *38* (2), 87–92.

(55) Konstantinov, I. A.; Broadbelt, L. J. Regression Formulas for Density Functional Theory Calculated1H And13C NMR Chemical Shifts in Toluene- D8. *J. Phys. Chem. A* **2011**, *115* (44), 12364–12372.

(56) Hansen, M. R.; Graf, R.; Sekharan, S.; Sebastiani, D. Columnar Packing Motifs of Functionalized Perylene Derivatives: Local Molecular Order Despite Long-Range Disorder. *J. Am. Chem. Soc.* **2009**, *131* (14), 5251–5256.

(57) Shaka, A. J.; Keeler, J.; Frenkiel, T.; Freeman, R. An Improved Sequence for Broadband Decoupling: WALTZ-16. *J. Magn. Reson. 1969* **1983**, *52* (2), 335–338.

(58) Khitrin, A.; Fung, B. M. Design of Heteronuclear Decoupling Sequences for Solids. *J. Chem. Phys.* **2000**, *112* (5), 2392–2398.

(59) Morcombe, C. R.; Zilm, K. W. Chemical Shift Referencing in MAS Solid State NMR. *J. Magn. Reson.* **2003**, *162* (2), 479–486.

(60) Hayashi, S.; Hayamizu, K. Chemical-Shift Standards in High-Resolution Solid-State Nmr (1) 13C, 29Si and 1H Nuclei. *Bull. Chem. Soc. Jpn.* The Chemical Society of Japan 公益社団法人 日本化学会 February 7, 1991, pp 685–687.

(61) Frisch, M. J.; Trucks, G. W.; Schlegel, H. B.; Scuseria, G. E.; Robb, M. A.; Cheeseman, J. R.; Scalmani, G.; Barone, V.; Mennucci, B.; Petersson, G. A.; Nakatsuji, H.; Caricato, M.; Li, X.; Hratchian, H. P.; Izmaylov, A. F.; Bloino, J.; Zheng, G.; Sonnenberg, J. L.; Hada, M.; Ehara, M.; Toyota, K.; Fukuda, R.; Hasegawa, J.; Ishida, M.; Nakajima, T.; Honda, Y.; Kitao, O.; Nakai, H.; Vreven, T.; Montgomery, J. A.; Peralta, J. E.; Ogliaro, F.; Bearpark, M.; Heyd, J. J.; Brothers, E.; Kudin, K. N.; Staroverov, V. N.; Keith, T.; Kobayashi, R.; Normand, J.; Raghavachari, K.; Rendell, A.; Burant, J. C.; Iyengar, S. S.; Tomasi, J.; Cossi, M.; Rega, N.; Millam, J. M.; Klene, M.; Knox, J. E.; Cross, J. B.; Bakken, V.; Adamo, C.; Jaramillo, J.; Gomperts, R.; Stratmann, R. E.; Yazyev, O.; Austin, A. J.; Cammi, R.; Pomelli, C.; Ochterski, J. W.; Martin, R. L.; Morokuma, K.; Zakrzewski, V. G.; Voth, G. A.; Salvador, P.; Dannenberg, J. J.; Dapprich, S.; Daniels, A. D.; Farkas, O.; Foresman, J. B.; Ortiz, J. V.; Cioslowski, J.; Fox, D. J. Gaussian 09, Revision D.01. Gaussian, Inc.: Wallingford, CT 2016.

(62) Sun, H.; Zhong, C.; Brédas, J.-L. Reliable Prediction with Tuned Range-Separated Functionals of the Singlet–Triplet Gap in Organic Emitters for Thermally Activated Delayed Fluorescence. *J. Chem. Theory Comput.* **2015**, *11* (8), 3851–3858.

(63) Takano, Y.; Houk, K. N. Benchmarking the Conductor-like Polarizable Continuum Model (CPCM) for Aqueous Solvation Free Energies of Neutral and Ionic Organic Molecules. *J. Chem. Theory Comput.* **2005**, *1* (1), 70–77.

(64) Sun, H.; Ryno, S.; Zhong, C.; Ravva, M. K.; Sun, Z.; Körzdörfer, T.; Brédas, J.-L. Ionization Energies, Electron Affinities, and Polarization Energies of Organic Molecular Crystals: Quantitative Estimations from a Polarizable Continuum Model (PCM)-Tuned Range-Separated Density Functional Approach. *J. Chem. Theory Comput.* **2016**, *12* (6), 2906–2916.

(65) Van Der Poll, T. S.; Zhugayevych, A.; Chertkov, E.; Bakus, R. C.; Coughlin, J. E.; Teat, S. J.; Bazan, G. C.; Tretiak, S. Polymorphism of Crystalline Molecular Donors for Solution-Processed Organic Photovoltaics. *J. Phys. Chem. Lett.* **2014**, *5* (15), 2700–2704.

(66) Coughlin, J. E.; Zhugayevych, A.; Bakus, R. C.; van der Poll, T. S.; Welch, G. C.; Teat, S. J.; Bazan, G. C.; Tretiak, S. A Combined Experimental and Theoretical Study of Conformational Preferences of Molecular Semiconductors. *J. Phys. Chem. C* **2014**, *118* (29), 140627161810001.

(67) McDowell, C.; Narayanaswamy, K.; Yadagiri, B.; Gayathri, T.; Seifrid, M.; Datt, R.; Ryno, S. M.; Heifner, M. C.; Gupta, V.; Risko, C.; Singh, S. P.; Bazan, G. C. Impact of Rotamer Diversity on the Self-Assembly of Nearly Isostructural Molecular Semiconductors. *J. Mater. Chem. A* **2018**, *6* (2), 383–394.

(68) Lodewyk, M. W.; Siebert, M. R.; Tantillo, D. J. Computational Prediction of ^{1}H and ^{13}C Chemical Shifts: A Useful Tool for Natural Product, Mechanistic, and Synthetic Organic Chemistry. *Chem. Rev.* **2012**, *112* (3), 1839–1862.

(69) Pierens, G. K. ^{1}H and ^{13}C NMR Scaling Factors for the Calculation of Chemical Shifts in Commonly Used Solvents Using Density Functional Theory. *J. Comput. Chem.* **2014**, *35* (18), 1388–1394.

(70) Benassi, E. Benchmarking of Density Functionals for a Soft but Accurate Prediction and Assignment of ^{1}H and ^{13}C NMR Chemical Shifts in Organic and Biological Molecules. *J. Comput. Chem.* **2017**, *38* (2), 87–92.

(71) Konstantinov, I. A.; Broadbelt, L. J. Regression Formulas for Density Functional Theory Calculated ^{1}H and ^{13}C NMR Chemical Shifts in Toluene-d_8. *J. Phys. Chem. A* **2011**, *115* (44), 12364–12372.

(72) Reddy, G. N. N. M.; Cook, D. S.; Iuga, D.; Walton, R. I.; Marsh, A.; Brown, S. P. An NMR Crystallography Study of the Hemihydrate of 2′, 3′-O-Isopropylidineguanosine. *Solid State Nucl. Magn. Reson.* **2015**, *65*, 41–48.

(73) Reddy, G. N. M.; Marsh, A.; Davis, J. T.; Masiero, S.; Brown, S. P. Interplay of Noncovalent Interactions in Ribbon-like Guanosine Self-Assembly: An NMR Crystallography Study. *Cryst. Growth Des.* **2015**, *15* (12), 5945–5954.